



# AAPG

# BULLETIN

VOLUME 99 • NUMBER 3 MARCH 2015 • ISSN 0149-1423







# AAPG | BULLETIN

VOLUME 99 • NUMBER 3 • MARCH 2015

## REGULAR FEATURES

|  |        |
|--|--------|
| Previews . . . . .                     | ii     |
| Staff Editors . . . . .                | iii    |
| Association . . . . .                  | iv     |
| House of Delegates . . . . .           | vi     |
| Instructions to Authors . . . . .      | 402    |
| Geoscience Meetings Calendar . . . . . | 466    |
| Electronic Submission . . . . .        | 498    |
| Officer Nominees . . . . .             | 584    |
| Education Calendar . . . . .           | (viii) |

**ON COVER** – Outcrops of the Cretaceous red bed mudstone and bleached sandstone of the Neuquén Group close to Barda González area, Neuquén Basin, Argentina. The reddish brown coloration of the Cerro Lisandro Formation mudstones grades upward to gray color in contact with the bleached sandstones (white in the picture) of the Portezuelo Formation. The image along the edge of the back cover is of the Portezuelo Formation at Barda González area, Neuquén Basin, Argentina. It shows bitumen impregnations in the bleached sandstone, like disseminated spots in cross bedding planes, in subhorizontal and discordant tubular and radial pipes, and as flames. Dendritic habit of bitumen develops toward the carbonate-cemented sandstones. See the related article by Pons et al., p.525, this issue of the *Bulletin*.

## GEOHORIZON

*Neoformed magnetic minerals as an indicator of moderate burial: The key example of middle Paleozoic sedimentary rocks, West Virginia*  
**Myriam Kars, Charles Aubourg, and Isabel Suárez-Ruiz . . . . .** 389

## ARTICLES

*Influence of mobile shale on thrust faults: Insights from discrete element simulations*  
**Sarah Dean, Julia Morgan, and J. P. Brandenburg . . . . .** 403

*The discovery of the Barmer Basin, Rajasthan, India, and its petroleum geology*  
**John Dolson, Stuart D. Burley, V. R. Sunder, V. Kothari, Bodapati Naidu, Nicholas P. Whiteley, Paul Farrimond, Andrew Taylor, Nicholas Direen, and B. Ananthakrishnan . . . . .** 433

*Reservoir quality of intrabasalt volcanoclastic units onshore Faroe Islands, North Atlantic Igneous Province, northeast Atlantic*  
**Jana Ólavsdóttir, Morten Sparre Andersen, and Lars Ole Boldreel . . . . .** 467

*Cretaceous Volcanic reservoirs and their exploration in the Songliao Basin, northeast China*  
**Pujun Wang and Shumin Chen . . . . .** 499

*Mineralogical signature of hydrocarbon circulation in Cretaceous red beds of the Barda González area, Neuquén Basin, Argentina*  
**M. J. Pons, A. L. Rainoldi, M. Franchini, A. Giusiano, N. Cesaretti, D. Beaufort, P. Patrier, and A. Impiccini . . . . .** 525

*The dynamic behavior of shallow marine reservoirs – Insights from the Pliocene of offshore North Trinidad*  
**Nigel E. Cross, Zana K. Williams, Arman Jamankulov, Candice E. Bostic, Valini C. Gayadeen, Helisaul J. Torrealba, and Elizabeth S. Drayton . . . . .** 555

### ACKNOWLEDGEMENTS—

AAPG thanks the **AAPG Foundation** for financial support of this issue of the *Bulletin*.  
 The AAPG Editor thanks the following reviewers for their work on papers in this issue:  
 Linda M. Bonnell, R. D. Elmore, William L. Esch, Jeffrey K. Geslin, Gary J. Hampson,  
 William A. Hill, Norman W. Kent, Joseph J. LAmbiase, Prasanta K. Mukhopadhyay,  
 Kenneth E. Peters, Antony D. Reynolds, Francois M. Roure, John H. Shaw,  
 and Rob van der Voo

# *Mineralogical signature of hydrocarbon circulation in Cretaceous red beds of the Barda González area, Neuquén Basin, Argentina*

**M. J. Pons, A. L. Rainoldi, M. Franchini, A. Giusiano, N. Cesaretti, D. Beaufort, P. Patrier, and A. Impiccini**

## **ABSTRACT**

The Portezuelo Formation is part of a red bed sequence in the Neuquén Basin assigned to the Neuquén Group (lower Cenomanian–middle Campanian). In outcrops of the Portezuelo Formation in the Barda González region, iron oxide and hydroxide cements are only preserved in the less permeable claystone layers. Paleomigration of hydrocarbons and formation waters along the most permeable layers bleached the rocks due to partial to total dissolution of cements and grains and formation of several authigenic minerals: (1) montmorillonite and pyrite in the medium- to fine-grained sandstones and mudstones, and (2) multi-stage calcite and pyrite in the coarse-grained sandstones and conglomerates. The  $\delta^{34}\text{S}_{\text{CDT}}$  (Canyon Diablo troilite) of  $-24.4$  to  $-60\%$  values in pyrite point to microbial reduction of a sulfate precursor. The oxidation of hydrocarbons and fluctuations in pH and carbon dioxide pressure caused by organic acids resulted in multiple stages of dissolution and precipitation of calcite. Calcite crystals host hydrocarbon-bearing fluid inclusions ( $\pm$  pyrite) with variable fluorescence color, indicating that hydrocarbon composition changed with time. The intermediate  $\delta^{13}\text{C}_{\text{PDB}}$  (Peedee belemnite) ( $-8.11\%$  to  $-8.52\%$ ) and  $\delta^{18}\text{O}_{\text{PDB}}$  ( $-9.76$  to  $-9.83\%$ ) isotope composition of calcites may have resulted from mixtures of  $^{13}\text{C}$ -rich  $\text{CO}_2$  after the dissolution of local calcrete with  $^{13}\text{C}$ -poor  $\text{CO}_2$  from oxidizing hydrocarbons.

This contribution provides for the first time key information to predict the distribution of authigenic minerals in reservoir rocks

## **AUTHORS**

M. J. PONS ~ *Consejo Nacional de Investigaciones Científicas y Técnicas; Centro Patagónico de Estudios Metalogenéticos, Universidad Nacional del Comahue, Buenos Aires 1400, CP8300, Neuquén, Universidad Nacional de Río Negro, Argentina; josefina.pons074@gmail.com*

María Josefina Pons obtained a bachelor's degree in geology and Ph.D. in natural sciences, specialized in economic geology at Facultad de Ciencias Naturales y Museo, Universidad Nacional de La Plata. Her current positions are mineralogy professor at Universidad Nacional del Comahue and Río Negro and assistant researcher of CONICET. Her main research lines are ore deposits related to Miocene Andean magmatism and sediment hosted Cu-V-U deposits associated to oil migration.

A. L. RAINOLDI ~ *Consejo Nacional de Investigaciones Científicas y Técnicas; Centro Patagónico de Estudios Metalogenéticos, Universidad Nacional del Comahue, Buenos Aires 1400, CP8300, Neuquén, Universidad Nacional de Río Negro, Argentina; Departamento de Geología, Universidad Nacional del Sur, Bahía Blanca, Argentina; analaurarl@hotmail.com*

Ana Laura Rainoldi belongs to the Centro Patagónico de Estudios Metalogenéticos (CPEM), is a Ph.D. candidate with a scholarship of CONICET, and a teaching assistant in sedimentology at the Universidad Nacional del Sur (Bahía Blanca, Argentina). Her Ph.D. project consists of the study of the cretaceous sediment-hosted stratiform Cu (V-U) deposits and its relationship with hydrocarbons in the Neuquén Basin, Argentina.

M. FRANCHINI ~ *Consejo Nacional de Investigaciones Científicas y Técnicas; Centro Patagónico de Estudios Metalogenéticos, Universidad Nacional del Comahue, Buenos Aires 1400, CP8300, Neuquén, Universidad Nacional de Río Negro, Argentina; mfranchini@speedy.com.ar*

Marta Franchini received her Ph.D. from Córdoba University and her postdoctoral training at Washington State University. She has worked as a researcher from CONICET leading metallogenic projects in several regions of Argentina. Her most important contributions include the development of new models for metal exploration in Argentina, the use of phyllosilicates in the exploration of porphyry Cu, providing useful information for processing of metals, the discovery of

Copyright ©2015. The American Association of Petroleum Geologists. All rights reserved.

Manuscript received September 12, 2013; provisional acceptance January 10, 2014; revised manuscript received February 10, 2014; revised manuscript provisional acceptance May 5, 2014; 2nd revised manuscript received May 13, 2014; final acceptance August 13, 2014.

DOI: 10.1306/08131413170

LREE-(Th-Nb) deposits and intracontinental alkaline-carbonatitic magmatism, and documenting the porphyry-epithermal transition in world class deposits and the interaction of hydrocarbon with red beds and Cu mineralization.

A. GIUSIANO ~ *Dirección Provincial de Hidrocarburos y Energía de la Provincia del Neuquén, Argentina; giusianoae@gmail.com*

Adolfo Giusiano has experience as a consultant geologist in regional mapping, economical evaluation of minerals deposits, and exploration of Cu and U in sedimentary rocks in Neuquén Basin and Cañadón Asfalto Basin. His current position is studies director of conventional and nonconventional hydrocarbon reservoirs at Mining and Hydrocarbons Undersecretary, Neuquén Province, Argentina.

N. CESARETTI ~ *Departamento de Geología, Universidad Nacional del Sur, Bahía Blanca, Argentina; ghcesar@criba.edu.ar*

Nora N Cesaretti is an adjunct professor in oil geology in the Geology Department of Universidad Nacional del Sur, Bahía Blanca, Argentina. She received the Lic. degree (B.S.) and her Ph. D. from Universidad Nacional del Sur. She did postdoctoral studies at Queen's University of Belfast (UK) in oil migration. Her research focus is on fluid inclusions on diagenetic environments linked to hydrocarbon.

D. BEAUFORT ~ *Université de Poitiers, IC2MP, CNRS-UMR 7285, Hydrasa, Bâtiment B08, Rue Albert Turpin, F-86022 Poitiers Cedex, France; daniel.beaufort@univ-poitiers.fr*

Daniel Beaufort is currently a professor of earth science at the University of Poitiers (France). He and his students are researching various aspects of the formation and transformation of clay minerals in natural systems. A consequent part of his research work has been in the clay mineral reactions during the sandstone diagenesis

P. PATRIER ~ *Université de Poitiers, IC2MP, CNRS-UMR 7285, Hydrasa, Bâtiment B08, Rue Albert Turpin, F-86022 Poitiers Cedex, France; patricia.patrier@univ-poitiers.fr*

Patricia Patrier received her Ph.D. in 1991 from Poitiers University (France). She spent four years in the industry and was enrolled as a lecturer at Poitiers University in 1996. She is currently a professor of mineralogy-geology. Her research interests include clay mineralogy, and alteration petrography. The main goal is to improve the use of clay mineral properties as petrogenetic indicators.

in the basin and improves understanding of the diagenetic history of the Portezuelo Formation.

## INTRODUCTION

The study area is located in the central region of the Dorsal de Huincul, including the Barda González, Puesto Espinoza, and Aguada Baguales oilfields (Figure 1). In this area, the Upper Cretaceous (upper Turonian–lower Coniacian, Leanza et al., 2004) subhorizontal conglomerates, pebble sandstones, sandstones, and mudstones of the Portezuelo Formation (Ramos, 1981) overlie middle–upper Turonian mudstones (Garrido, 2010) of the Cerro Lisandro Formation (Ramos, 1981). The Portezuelo and the Cerro Lisandro Formations are part of a thick continental sequence within the Neuquén Group (lower Cenomanian–middle Campanian, Leanza et al., 2004). In contrast to the reddish brown color of the Neuquén Group rocks at regional scale in the basin, rocks in the area of Barda González are commonly bleached. Hydrocarbons migrating through the most permeable layers partially or completely dissolved the previous cements and grains and facilitated precipitation of calcite (multistage cementation), montmorillonite, and pyrite. Several published examples document the spatial relationship of bleached red beds and the movement of hydrocarbons through rocks (Moulton, 1926; Levandowski et al., 1973; Segal et al., 1986; Surdam et al., 1993; Sanford, 1995; Foxford et al., 1996; Britton, 1998; Chan et al., 2000; Garden et al., 2001; Beitler et al., 2005) and in laboratory experiments (Shebl and Surdam, 1996). Bleaching of the Neuquén Group sandstones was identified as early as 1951, when petroleum geologists referred to grayish-white pyrite-rich sandstones in several subsurface cuttings samples from the Barda González oil field (drill hole NBG1, YPF unpublished report, 1951). Similar alteration was observed in the wall rock of the asphaltite veins in the Neuquén Basin (Parnell and Carey, 1995). In numerous oil fields located in the northeast region of the Neuquén Basin, geologists described white to grayish reservoir rocks of the Neuquén Group (Manacorda et al., 2002). Reactions between hydrocarbons and sedimentary rocks have been invoked to explain the bleached nature of Cretaceous sandstones of the Huincul Formation in the Neuquén Basin (Giusiano et al., 2006, 2008; Giusiano and Bouhier, 2009; Pons et al., 2009, 2011; Rainoldi et al., 2012, 2014).

The purpose of this contribution is to establish the mineralogical signature of the hydrocarbon circulation in Cretaceous red beds of the Barda González area. In this study, petrography and secondary mineral crystal chemistry were used to decipher the relationship between diagenetic processes, the migration of



hydrocarbons and associated basinal fluids, and the sequence of mineral precipitation in order to reconstruct the complex diagenetic history of the Portezuelo Formation.

## GEOLOGICAL AND TECTONIC SETTING

The Neuquén Basin (Figure 1) extends over 124,000 km<sup>2</sup> (47,876.67 mi<sup>2</sup>) and is located in the foothills of the Andes.

The Neuquén Basin started as a northwest-rifting system during the Triassic and evolved from a back-arc basin during the Mesozoic with a complex tectonic history (Digregorio et al., 1984; Macellari, 1988; Legarreta and Uliana, 1991) to a foreland basin during the Late Cretaceous (Ramos, 1981, 1999; Tunik et al., 2010). The basement consists of plutonic, pyroclastic, and volcanoclastic rocks of the Choiyoi Group (Stipanovic et al., 1968), and the basin infill consists of more than 7000 m (23,000 ft) of Upper Triassic–lower Cenozoic marine, evaporites and continental sedimentary rocks (Figure 2). The sedimentary rocks in this basin resulted from several regional transgressions of the Pacific Ocean, mainly because of the post-rift thermal subsidence and eustatic rise in the sea level (e.g., Gulisano et al., 1984; Legarreta and Gulisano, 1989; Legarreta et al., 1993; Legarreta and Uliana, 1991, 1996a, b, 1998; Franzese et al., 2003). This sedimentary succession culminated with Campanian–Maastrichtian sediments formed by a transgression of the Atlantic Ocean (Uliana and Biddle, 1988). All of these regional transgressive–regressive cycles controlled the configuration of the Neuquén Basin and favored the development of oil and gas source rocks, reservoir rocks, and seal rocks (Figure 2, Schiuma et al., 2002; Legarreta et al., 2003; Villar et al., 2005). The basin hosts the most important hydrocarbon fields of Argentina (Uliana et al., 1999; Schiuma et al., 2002).

The study area is located on the main fault of the Dorsal de Huincul morphological-structural unit (Figure 1B). This unit is a structural lineament of regional scale developed at 39° south latitude, with east–west strike that extends 270 km (167.77 mi; Figure 1), defining the northern boundary of Argentinean Patagonia with the Neuquén Basin (Ramos et al., 2004; González et al., 2011). This structure was interpreted as a dextral fault zone with both transpressive and transtensive segments due to changes in the fault zone trend (Płoszkiewicz et al., 1984). Silvestro and Zubiri (2008) proposed that this ridge is the result of an oblique northwest–southeast convergence during the Early Jurassic and Cretaceous. This compressive event produced new structures and reactivated some of the previous rift system developed between the North Patagonian Massif in the southeast and the Neuquén Basin in the northwest (Cruz et al., 2002; Silvestro

A. IMPICCINI ~ *Centro Patagónico de Estudios Metalogenéticos, Universidad Nacional del Comahue, Buenos Aires 1400, CP8300, Neuquén, Universidad Nacional de Río Negro, Argentina; aimpicc@gmail.com*

Agnes Impiccini obtained a degree in geology and a Ph.D in natural sciences at Facultad de Ciencias Naturales y Museo, Universidad Nacional de La Plata. She has developed teaching and research activities in petrophysical conditions of rocks, geology of oil and gas, and clay minerals in ore deposits at Universidad Nacional del Comahue since 1986.

## ACKNOWLEDGEMENTS

This research represents part of a project financed by FONCYT (PICT no. 2010-2608; PICT-prh-2008-00093, 1120), CONICET (PIP no. 1083) and the European Commission through its Erasmus Mundus program. We express our appreciation to Ariel Testi, Eduardo Bouhier, and the staff of Orión del Sur Mining Company for site access, logistic support, and help during the field work. We are especially grateful to Osvaldo Carbone and Martín Cevallos for their excellent suggestions and discussion that helped to improve this manuscript, to Pluspetrol S.A. Company for access to water formation chemistry analyses, to Ildefonso Armenteros and Clemente Recio Hernández for support and comments during the cathodoluminescence and isotope stable analyses, and to Valentin Rubin for his advice on the interpretation of mid-infrared (MIR) spectra, and to Maisa Tunik for her collaboration in the provenance clast analyses. We thank the AAPG reviewers Kenneth Peters, William Esch, David Awwiller, and Michael Sweet for their constructive reviews, which led to further improvement of this manuscript.

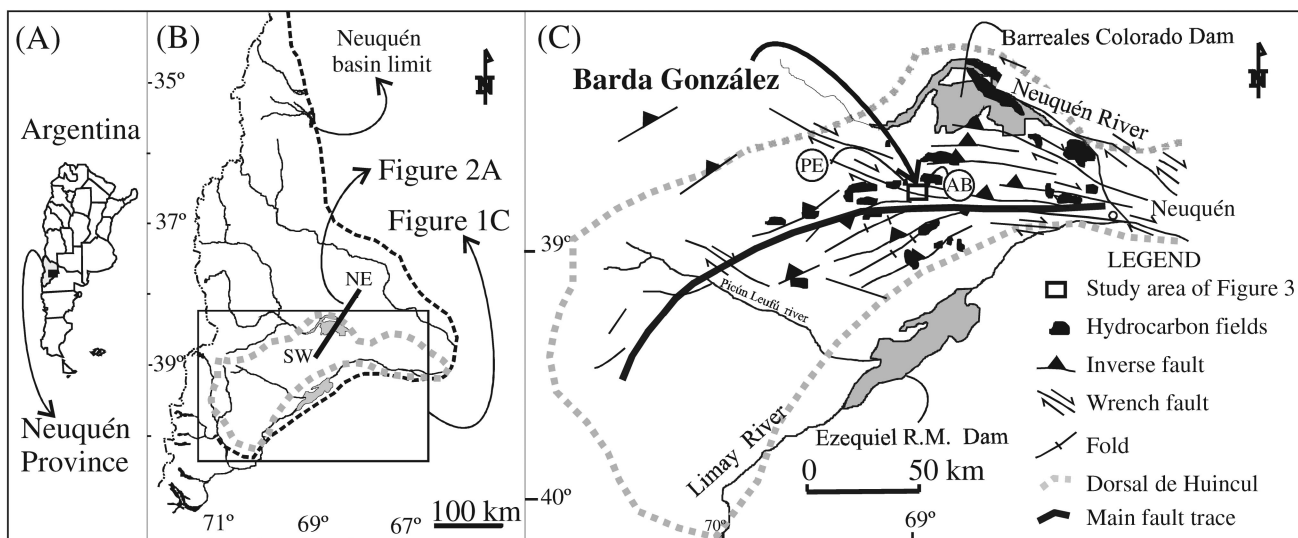


**Figure 1.** (A) Location map of the Neuquén Basin and (B) Dorsal de Huincul, with (C) the distribution of oilfields and location of Barda González, Puesto Espinoza (PE), and Aguada Baguales (AB) oilfields (modified after Silvestro and Zubiri, 2008).

and Zubiri, 2008). Most of these faults have a deep origin and die out at the base of the Vaca Muerta Formation (Tithonian; Figure 2). Other faults closer to the main fault originate in shallower levels and cross cut the base of the Neuquén Group (Figure 2; Schiuma et al., 2002; Silvestro and Zubiri, 2008).

Solid hydrocarbons (bitumen) have been described in the fluvial deposits of the Neuquén Group in the Dorsal de Huincul region (Giusiano et al., 2006; 2009; Pons et al., 2009, 2011; Rainoldi et al., 2012). These sedimentary rocks represent the first fill of synorogenic fluvial deposits in the foreland basin during the Late Cretaceous (Legarreta and Uliana, 1998; Ramos and Folguera, 2005; Tunik et al., 2010) and cover almost all of the central and eastern Neuquén Basin reaching up to 1300 m (4265 ft) thick in the embayment zone (Cazau and Uliana, 1972). The Neuquén Group unconformably overlies the continental sedimentary rocks of the Rayoso Formation (Aptian–Albian) and is covered by marine deposits of the Malargüe Group (Figure 2; lower Maastrichtian–upper Campanian). The Neuquén Group has been divided into three subgroups: the Río Limay subgroup with Candeleros, Huincul, and Cerro Lisandro formations; the Río Neuquén subgroup with Portezuelo and Plottier formations; and the Río Colorado subgroup with Bajo de la Carpa and Anacleto formations (Ramos,

1981; Figure 2). They consist of fluvial, lacustrine, and eolian red bed sequences of fine- to coarse-grained sandstones and conglomerates interbedded with claystones and mudrocks (Legarreta and Uliana, 1998).

## GEOLOGY OF THE STUDY AREA

The Barda González area is located above one of the master east–west faults of the Dorsal de Huincul (Figures 1, 2). This fault developed during the Jurassic–Cretaceous northwest–southeast oblique convergence in a block defined by two subparallel northwest–southeast normal faults in the previous Triassic rift. The evolution of the stress field in the Barda González area was influenced by an initial northwest–southeast extensional regime during the Triassic. Oblique northwest–southeast convergence during the Early Jurassic and Early Cretaceous caused inversion of the previous normal fault and new inverse and wrench lateral faults depending on the obliquity of the stress with the previous structures. This convergence also caused a local north–south compression that formed open fractures with this orientation during thermal subsidence of the rift (Silvestro and Zubiri, 2008). From the Kimmeridgian to the Holocene, the Andean orogeny generated a northwest–southeast stress field



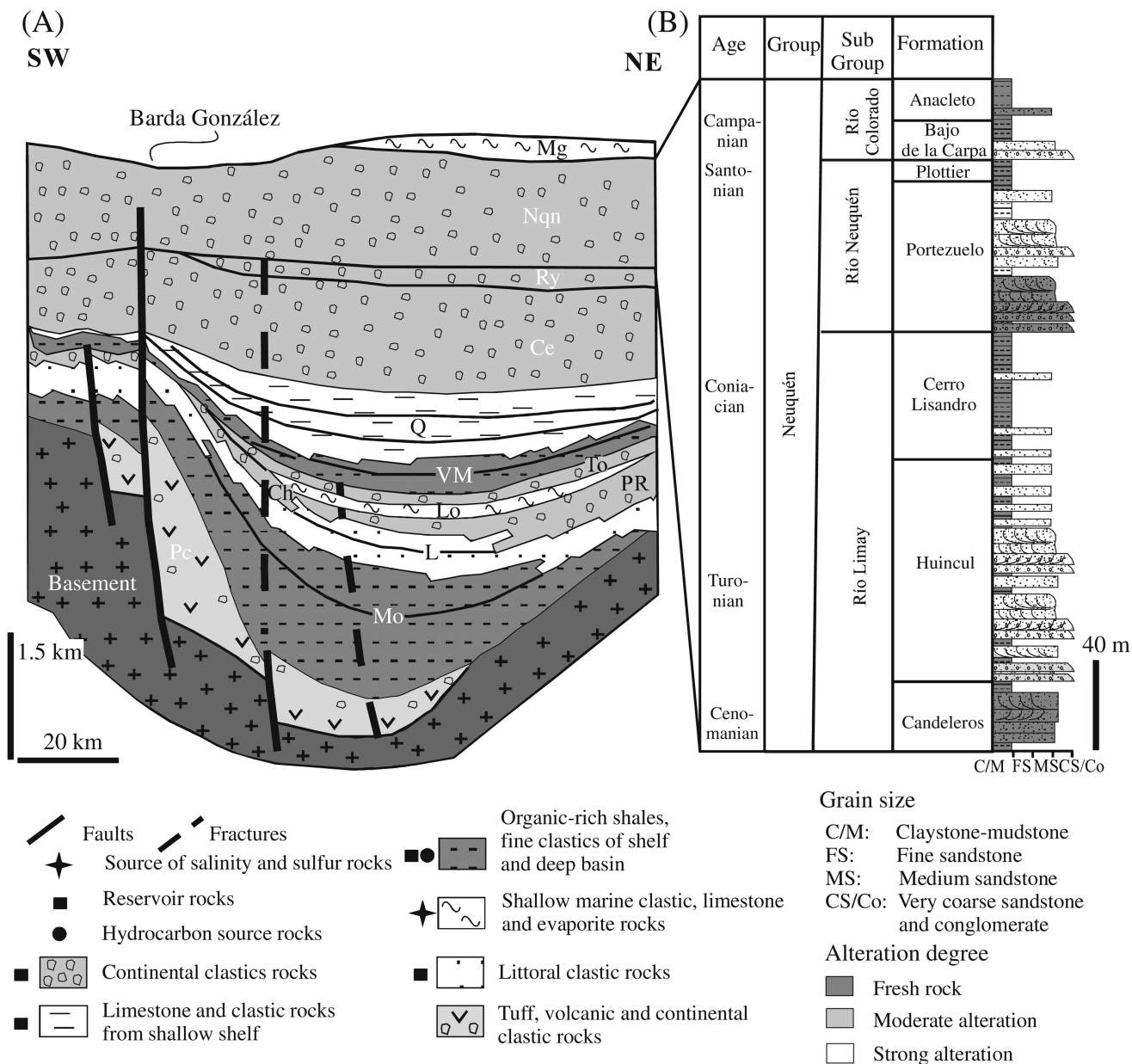


**Figure 2.** (A) Northeast–southwest cross section showing the stratigraphic succession of the Neuquén Basin with the Paleozoic (granitic basement); Triassic (Pre-Cuyo Formation; Pc), Jurassic (205–142 Ma: Los Molles [Mo], Lajas [L], Challacó [Ch], Punta Rosada [PR], Lotena [Lo], Tordillos [To] Formations), Cretaceous (142–65 Ma: Vaca Muerta [VM], Quintuco [Q], Centenario [Ce], Rayoso [Ry] Formations and Neuquén [Nqn] and Malargüe [Mg] Groups) filling rocks and the main structures of the Dorsal de Huincul region (modified after Cruz et al., 2002); (B) detailed stratigraphic column of the Neuquén Group (modified after Giusiano et al., 2008).

(Silvestro and Zubiri, 2008) that resulted in reactivation of previous structures and deformation of the Neuquén Group beds during the Miocene (Mosquera and Ramos, 2006).

In this region, flat layers of the Huincul, Cerro Lisandro, and Portezuelo Formations are exposed (Figure 3). The upper section of the Huincul

Formation crops out in the southern half of the study area. The contact with the Cerro Lisandro Formation is sharp and can be identified by the first reddish-brown claystones and siltstones (Figures 3, 4). The Cerro Lisandro Formation grades upward to coarser-grained beds, and the contact with the Portezuelo Formation is transitional. The last two formations

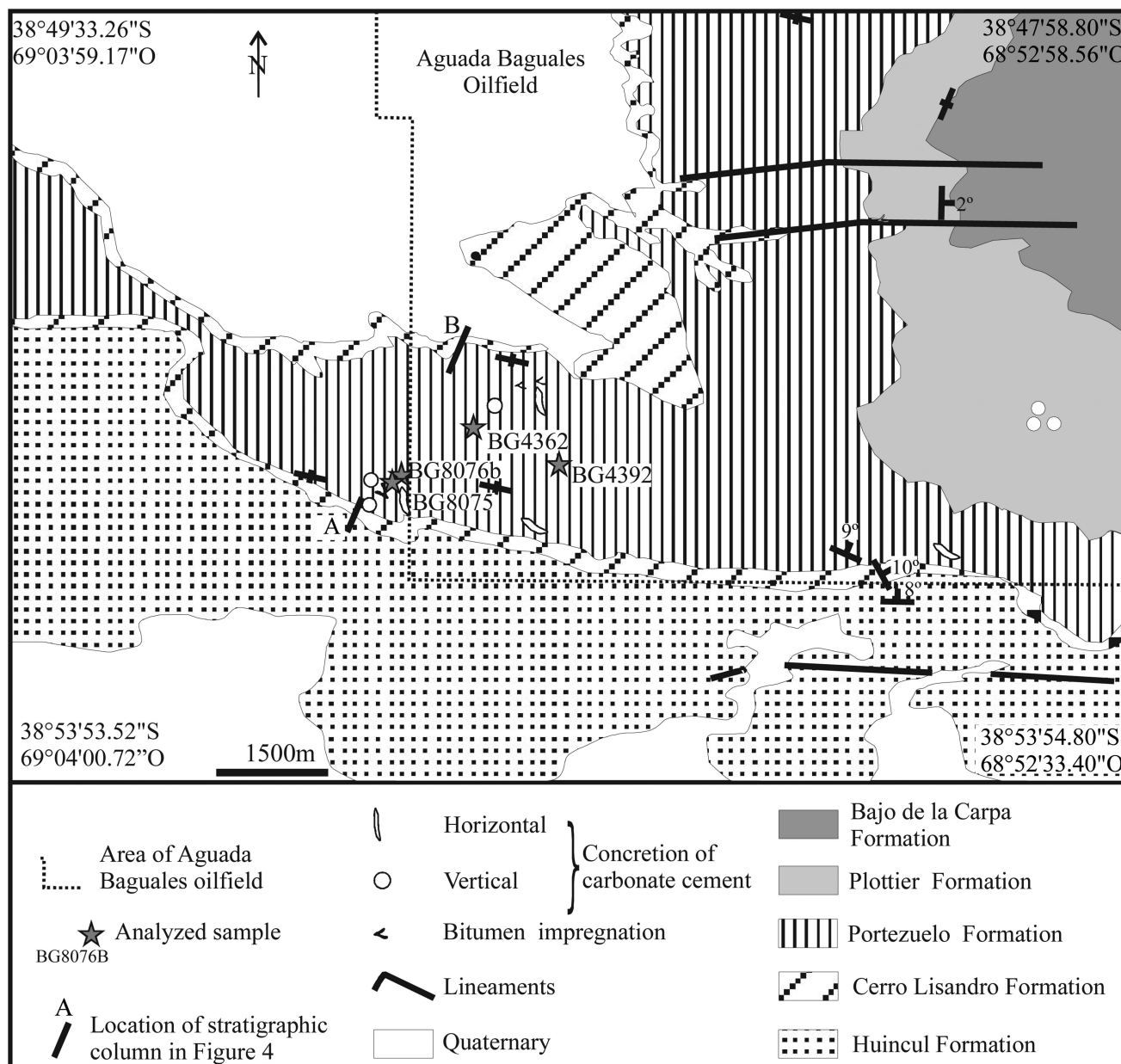


**Figure 3.** Geologic map of the Barda González area. A and B are the locations of the stratigraphic columns in Figure 4.

occur as a lenticular east–west plateau 9 km (5.59 mi) long, 2 km (1.24 mi) wide, and 87 m (285.43 ft) thick (Figures 3, 4). Toward the northeast of the study area, there is a gradational contact between the Portezuelo and Plottier formations, and the latter is overlain by the Bajo de la Carpa Formation (Figure 3).

Near the Barda González area, the Huincul Formation consists of interbedded gray to grayish white, medium- to coarse-grained sandstones and conglomerates with moderately to well-sorted subangular clasts. The conglomerate layers are

rich in gray mud chips. The sandstones consist of volcanic fragments (25–40%), quartz (15–30%), feldspar (5–30%), and traces of muscovite. The volcanic lithic clasts contain magnetite as micro-inclusions. The mud (clay) chips of the conglomerate layer are ellipsoidal and contain quartz (44%), clay minerals (34%), and feldspar (22%).

The Cerro Lisandro Formation crops out in the lower portion of the plateau (Figures 3, 4) and consists of reddish-brown claystones (Figure 4H) with intercalated gray mudrocks and coarsening upward



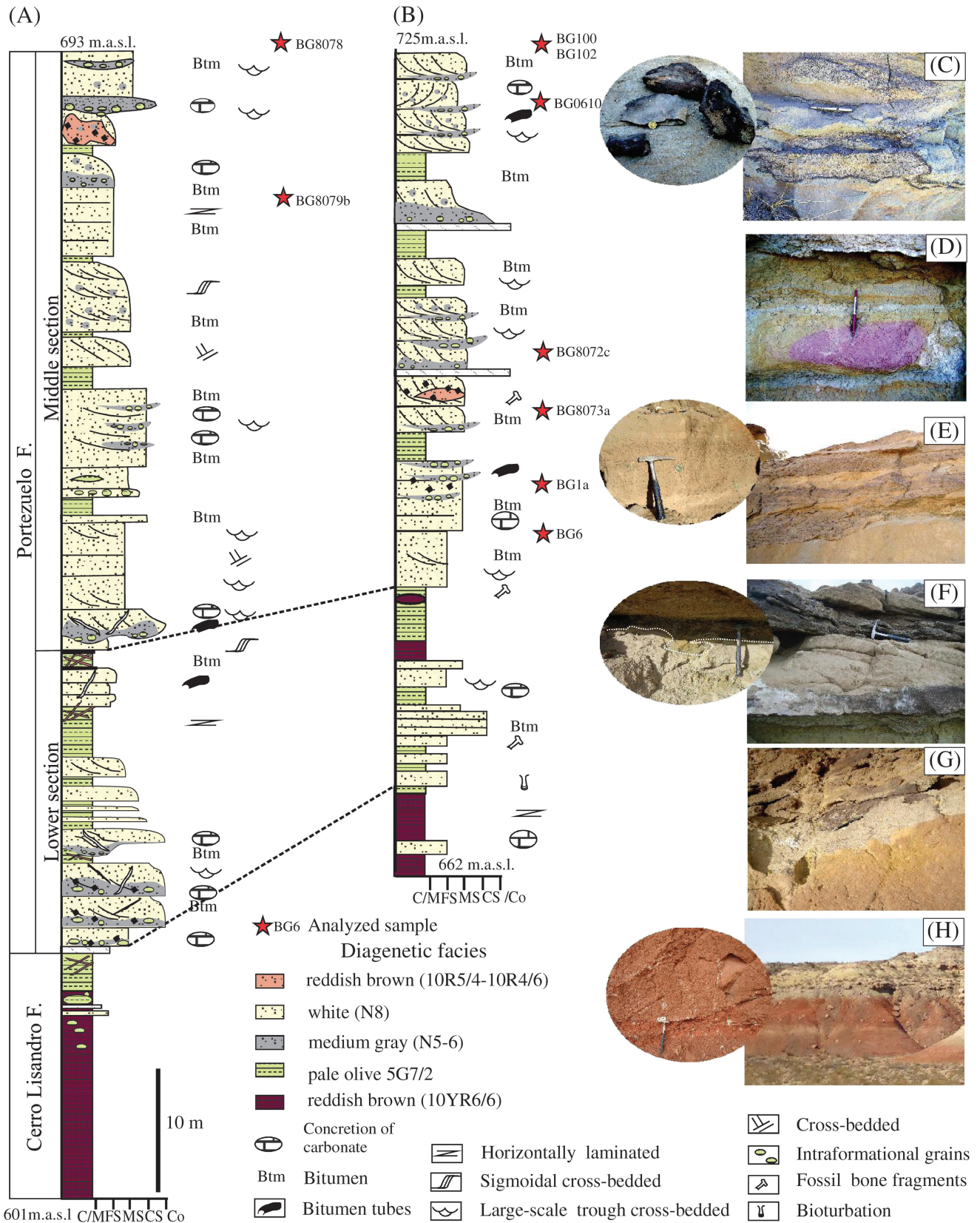


**Figure 4.** (A–B) Stratigraphic columns of the Portezuelo Formation showing the distribution of the different diagenetic facies and (C–H) photography from outcrops (see text for further explanation).

medium-grained sandstones. The claystone contains 90% clay minerals (illite, kaolinite, and mixed-layer illite-smectite in variable proportions), 8%–10% quartz, 0–2% feldspar, and traces of calcite. The contact between the Cerro Lisandro Formation and the base of the Portezuelo Formation is defined by the first thick sandstone beds (Figure 4).

## SAMPLES AND ANALYTICAL METHODS

The lithofacies characterization and the architectural elements were based mainly on Miall (1996). Color variations were cataloged using the Munsell rock color chart. To characterize the petrography of the Portezuelo Formation, samples of conglomerates (40), coarse- to fine-grained sandstones (25), and mudrocks (2) were systematically collected from two stratigraphic sections and outcrops (Figures 3, 4). Thin sections ( $n = 50$ ) were made for petrography of the sandstone samples. Six thin sections were made using blue epoxy to estimate their porosity (Table 1). A minimum of 400 framework grains and intergranular space components were counted per thin section for quantitative petrographic analysis using the Gazzi-Dickinson method (Gazzi, 1966; Dickinson, 1970; Ingersoll et al., 1984). The mineralogical study of mudrocks was carried out by X-ray diffraction (XRD). The  $<2 \mu\text{m}$ -size fraction of the rocks was collected by sedimentation, and clay minerals were characterized from XRD patterns of air-dried oriented preparations after ethylene glycol solvation and heating for 2 hr at  $500^\circ\text{C}$ , respectively. The XRD was performed on a Bruker D8 Advance diffractometer equipped using Ni-filtered  $\text{Cu K}\alpha_{1,2}$  radiation. Bulk composition was determined using the powder diffraction method. Quantitative clay analyses were carried out using the mineral intensity factor (MIF) method (Moore and Reynolds, 1997). Relative abundance of illite, smectite, chlorite, and kaolinite in the clay-size fraction was estimated from integrated peak intensities on diffraction patterns of oriented clays on glass slide X-ray mounts. The method (Moore and Reynolds, 1997) gives the relative proportions of the clay minerals normalized to 100%. Infrared analyses were carried out on selected samples as a complementary technique for the determination of clay mineralogy at IC2MP Laboratory,

**Table 1.** Portezuelo Formation Provenance Clast Analyses

| Parameters                  | Sample Number |              |              |              |              |              |
|-----------------------------|---------------|--------------|--------------|--------------|--------------|--------------|
|                             | BG 8076b      | BG 1a        | BG 8075      | BG 8073a     | BG 8079b     | BG 6         |
| Type of Grains              |               |              |              |              |              |              |
| Qzmo                        | 7.0           | 12.0         | 11.5         | 9.5          | 10.5         | 4.1          |
| Qzmr                        | 42.0          | 40.8         | 40.3         | 46.3         | 32.0         | 36.5         |
| Qzp3                        | 2.8           | 1.3          | 1.5          | 3.3          | 2.3          | 1.0          |
| Qzp2                        | 0.0           | 0.3          | 0.0          | 0.0          | 0.0          | 0.0          |
| Qzp1                        | 0.3           | 0.5          | 0.0          | 0.0          | 0.8          | 0.0          |
| Om                          | 0.0           | 0.0          | 0.3          | 0.0          | 0.0          | 0.8          |
| Op                          | 0.8           | 1.3          | 0.0          | 0.0          | 1.3          | 0.0          |
| P                           | 3.3           | 2.0          | 7.5          | 0.0          | 1.0          | 19.1         |
| Ms                          | 2.8           | 2.8          | 3.0          | 1.5          | 0.5          | 0.5          |
| Ls                          | 6.3           | 0.0          | 0.0          | 0.0          | 13.3         | 0.0          |
| Lps                         | 0.8           | 0.0          | 0.0          | 0.0          | 0.0          | 0.0          |
| Lpv                         | 2.5           | 1.5          | 1.0          | 5.0          | 1.0          | 3.9          |
| Lm                          | 3.0           | 3.3          | 2.0          | 0.5          | 3.0          | 0.0          |
| La                          | 2.0           | 4.8          | 10.3         | 6.5          | 6.5          | 1.4          |
| Pl                          | 10.8          | 11.0         | 6.5          | 10.8         | 11.8         | 9.5          |
| Mc                          | 0.8           | 0.3          | 1.0          | 0.3          | 0.5          | 4.6          |
| Afs                         | 6.3           | 7.3          | 11.5         | 11.0         | 4.5          | 10.5         |
| Btm, Co                     | 4.3           | 2.5          | 2.8          | 0.8          | 1.0          | 0.0          |
| Cb                          | 1.8           | 0.0          | 0.0          | 0.0          | 7.5          | 0.0          |
| Cl                          | 3.0           | 8.8          | 1.0          | 4.8          | 2.8          | 8.5          |
| <i>Total</i>                | <i>100.0</i>  | <i>100.0</i> | <i>100.0</i> | <i>100.0</i> | <i>100.0</i> | <i>100.0</i> |
| Qz                          | 52.0          | 54.8         | 53.3         | 59.0         | 45.5         | 41.6         |
| Fsp                         | 17.8          | 18.5         | 19.0         | 22.0         | 16.8         | 24.6         |
| Lt                          | 12.5          | 4.8          | 3.0          | 5.5          | 17.3         | 3.9          |
| <i>Total</i>                | <i>82.3</i>   | <i>78.0</i>  | <i>75.3</i>  | <i>86.5</i>  | <i>79.5</i>  | <i>70.1</i>  |
| Recalculated values to 100% |               |              |              |              |              |              |
| Qz                          | 63.2          | 70.2         | 70.8         | 68.2         | 57.2         | 59.3         |
| Fsp                         | 21.6          | 23.7         | 25.2         | 25.4         | 21.1         | 35.1         |
| Lt                          | 15.2          | 6.1          | 4.0          | 6.4          | 21.7         | 5.6          |

Afs = alkaline feldspar; Btm = bitumen; Cb = carbonates cement; Cl = argillaceous cement; Co = other cements; La = altered minerals; Lm = metamorphic lithic grains; lps = pseudomatrix; Lpv = plutonic and paleovolcanic lithic grains; Ls = sedimentary lithic grains; Mc = microcline; Ms = mica grains; Om = other minerals; Op = opaque mineral grains; Pl = plagioclase; P = porosity; Qzp1 = polycrystalline quartz with two subgrains; Qzp2 = polycrystalline quartz with three subgrains; Qzp3 = polycrystalline quartz with more than three subgrains. Recalculated values =  $Qz = (Qzmr + Qzmo + Qzp1 + Qzp2 + Qzp3)$ ;  $Fsp = (Mc + Pl + Afs)$ ;  $Lt = (Lvf + Lvp + Lpi + Ol + Ls + La + Lp)$ .

Université de Poitiers, France. Middle-infrared (MIR) spectra ( $400$  to  $4000 \text{ cm}^{-1}$ ) of clays were acquired from KBr pellets using a Nicolet 760 FT-IR spectrometer equipped with a potassium bromide (KBr) beam splitter and DTGS-KBr detector. The resolution was set at  $4 \text{ cm}^{-1}$  with co-addition of



100 scans. The KBr pellets were prepared using 1 mg of sample for 150 mg of KBr powder. The mixture was crushed in a mortar and placed in a hydraulic press for 5 min (<8 tons) before drying at 120°C (248°F).

Two thin sections of sandstones with abundant calcite cement were selected for cathodoluminescence analyses using a cold cathode (CL8200mk3) coupled to a Nikon Labophot microscope with vacuum chamber on the stage at the Geology Department, Facultad de Ciencias, Universidad de Salamanca. The calcite cements with different luminescent response were analyzed by electron microprobe (Cameca SX-50) with five wavelength dispersive spectrometers (WDS) and one energy dispersive spectrometer (EDS) silicon drift type detector (SDD) at the Universidad de Barcelona. Representative samples with clay cement were selected for scanning electron microscopy (SEM) using small, freshly fractured bulk rock samples and thin polished sections that were coated with carbon. Quantitative chemical analysis of clay cement was performed using JEOL 5600 LV SEM equipped with an EDS (BRUKER XFlash 4030 silicon drift detector) at IC2MP Laboratory, Université de Poitiers, France. Analytical conditions were 15 kV, 1 nA, a counting time of 60 s and a working distance of 16.5 mm. The standards used for EDS consisted of albite (Na, Al, Si), almandine (Mg, Fe), diopside (Ca), orthoclase (K) and spessartite (Mn). Matrix corrections were performed using integrated programs (a PhiRhoZ correction). The reproducibility of the standard analyses was ~1.5% for all of the elements, except Na, which was ~3%.

Four samples that preserved calcite cements were selected for fluorescence and fluid inclusion analysis. Samples were analyzed with a polarization-fluorescence Nikon Eclipse 50i microscope. Microthermometric analyses of fluid inclusions ( $n = 20$ ) in calcite were carried out using Linkam (-180°/+600°C [-292°/+1112°F]) cooling-heating stages at the Fluid Inclusion Laboratory of the Departamento de Geología of the Universidad Nacional del Sur, Bahía Blanca, Argentina.

Selected carbonates (4) and sulfides (5) were analyzed for  $\delta^{18}\text{O}$ ,  $\delta^{13}\text{C}$ ,  $\delta^{34}\text{S}$  as appropriate, at the Servicio de Isótopos Estables, Universidad de

Salamanca, using two SIRA-II gaseous source dual inlet mass spectrometers. Samples were prepared by handpicking and microdrilling, and then converted to a suitable gas in the gas extraction lines. Carbonates were treated prior to the isotope analyses using an Asher model K1050X EMITEC to eliminate traces of bitumen and organic matter through combustion at low temperature in the presence of oxygen plasma. The  $\text{CO}_2$  was produced by reaction with 100%  $\text{H}_3\text{PO}_4$  (McCrea, 1950). For conventional  $\delta^{34}\text{S}$  analysis of sulfide minerals,  $\text{SO}_2$  was produced by reaction of the sulfide or sulfate minerals with an oxidant ( $\text{Cu}_2\text{O}$ ) at elevated temperature (1000 to 1200°C [1832 to 2192°F]) under vacuum (Holt and Engelkemeier, 1970; Hair et al., 1973; Coleman and Moore, 1978). Isotopic results are reported in  $\delta$  notation relative to SMOW (standard mean ocean water) for O, PDB (Peedee belemnite) for C and O, and Canyon Diablo troilite (CDT) for S. Repeat analyses of international and internal reference materials gave average reproducibility better than  $\pm 0.02\%$  for  $\delta^{13}\text{C}$  and  $\pm 0.12\%$  for  $\delta^{18}\text{O}$  in carbonates,  $\pm 0.2\%$  for  $\delta^{18}\text{O}$  by laser fluorination, and  $\pm 0.1\%$  for  $\delta^{34}\text{S}$ .

Two outcrop samples (BG08072c and BG102) were submitted to Weatherford Laboratories for geochemical analysis to determine the source rock for the entrained bitumen. Portions of the outcrop rocks that appeared to contain the most bitumen were crushed and extracted using carbon disulfide. The extract was concentrated and then analyzed by gas chromatography. Unfortunately, because the first sample (BG08072c) collected contained too little bitumen for further analysis, only the second sample (BG102) was chosen, and the process was repeated. The second sample (BG102) was separated by liquid chromatography into saturate, aromatic, resin and asphaltene fractions. The saturate and aromatic fractions were analyzed for biological marker compounds (biomarkers). The biomarkers from the first sample (BG08072c) were measured using the whole oil.

## RESULTS

In the study area, the lower and middle sections of the Portezuelo Formation outcrop with a total thickness of 60 m (196.85 ft; Figures 3, 4). Both sections have

lower proportions of coarse-grained facies toward the east, and they can be differentiated by the ratio of coarse- to fine-grained facies. The coarse- to fine-grained ratio is higher in the middle section (Figure 4). These two sections consist of medium-grained sandstones (Sh, St, Sr) and subordinate conglomerates (0.4–2.5 m or 1.31–8.2 ft thick), rich in intraclasts of claystone and siltstone (Gm, Gh, Gp, Gt), interbedded with beds of massive micaceous sandstones (Sm) and mudrocks (<1 to 5 m [ $<3.28$  to 26.25 ft] thick) in fining-upward sequences (Fm) (Figure 4D). The sandstones and conglomerates form sheet-like and lenticular packages with planar erosive bases and medium-scale trough cross-bedding (Figure 4E, F) that commonly shows paleoflows with northeast and southwest trends. They contain fragments of fossilized tree trunks and vertebrate bones. The mudrocks form tabular and massive beds up to 3 m (9.84 ft) thick in the lower section and discontinuous lenses with planar cross-bedding upward. Some of these mudrocks show bioturbation. Commonly, the mudrocks, overlain by the thickest sandstones, show deformation due to water escape structures (Figure 4F).

## Petrography

The coarsest grained facies (sandstones to conglomerates) exhibit mature to submature textures dominated by moderately to well-sorted subangular to subrounded grains. They vary in color from white to yellowish-gray, medium-gray, and reddish-brown, and consist of 57%–70% quartz, 21%–35% feldspar, 4%–22% lithics, with <1% micas (Table 1), tourmaline, monazite, rutile, and zircon as accessory minerals. The feldspars are dominantly potassic (microcline, perthitic orthoclase) with subordinate oligoclase-andesine. The most common lithic clasts consist of volcanic rock fragments with microlithic and felsitic textures and metamorphic rock fragments of quartz–chlorite–muscovite schist. Some of the detrital feldspars and lithic fragments have been hydrothermally altered and partially replaced by illite and chlorite prior to their deposition. Frequently, the base of each layer is dominated by a monomictic conglomerate rich in clay chips. The fine-grained sandstones are characterized by abundant mica (2%–3%).

All of the sandstones from the Portezuelo Formation are classified as lithic feldarenite and feldspathic litharenite, following the classification of Folk et al. (1970).

The claystones and siltstones of the Portezuelo Formation show reddish-brown (10YR6/6), yellowish-gray (5GY8/1), and pale olive (5GY7/2) colors. They consist of clay minerals (59 to 88 vol. %), including inherited hydrothermal illite and chlorite, quartz (14–23%), plagioclase (oligoclase-andesine, 9–18%), and K-feldspar (1%).

## Diagenesis and Alteration of Sandstones and Conglomerates

Bleaching of sedimentary rocks related to the dissolution of the iron oxide and hydroxide cements is a common feature in the area. The primary reddish color of the rocks is only preserved in the less permeable reddish-brown (10YR6/6) and thickest claystone layers (Figure 4). Based on colors of the Portezuelo Formation rocks, four facies were differentiated: (1) white (N8) sandstones, (2) reddish-brown sandstones (10R5/4–10R4/6), (3) yellowish-gray (5Y8/1) sandstones, and (4) medium-gray (N5–N6) coarse to pebble sandstones and conglomerates (Figure 4). The white and yellowish-gray facies are observed in the medium- to coarse-grained sandstones. The medium-gray facies is generally at the base of the thickest sandstone and conglomerate layer (Figure 4A, B, F). The reddish-brown facies outcrops at a height of 690 m (2264 ft) above sea level in the plateau. The contact between this reddish-brown and the other facies (white to yellowish-gray) is irregular; in some places, patches of reddish facies are enclosed within the white, bleached facies (Figure 4A, B, D).

The white and the reddish-brown facies are composed of very permeable and friable sandstones with more than 15 vol. % intergranular porosity (primary and secondary) with oversize pores resulting from selective leaching of detrital grains. The quartz clasts and polycrystalline lithic quartz commonly show randomly oriented microfractures (Figure 5A). Micas are more abundant in the finest grained sandstones and typically show slightly ductile deformation as a result of diagenetic mechanical compaction. Feldspars and volcanic fragments are partially dissolved. The

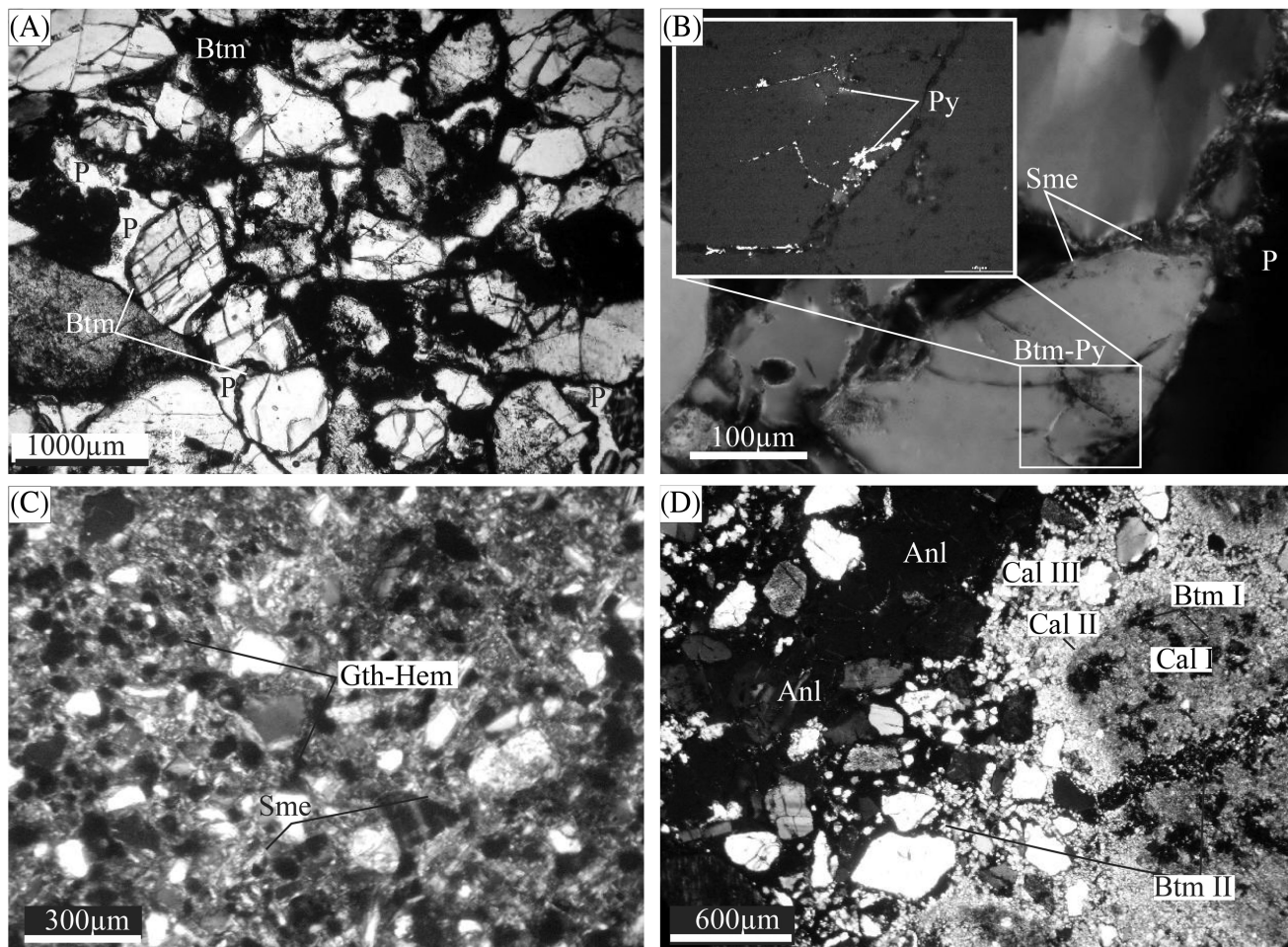


**Figure 5.** Photomicrographs of sandstone facies developed during deposition, diagenesis, and alteration. White facies: (A) with bitumen coatings grains and fractures, (B) authigenic smectite (Sme) as rims, and bitumen and pyrite fill the fractures of the clasts, (C) sandstones with abundant smectite cement and disseminated euhedral pyrite partially altered to goethite and hematite, (D) facies with bitumen impregnations and the floating grain texture as a result of dissolution and replacement of previous cement grains by calcite and analcite. Anl = analcite; Btm I, II = bitumen I, II; Cal I, II, III = calcite I, II, III; Gth = goethite; Hem = hematite; Sme = smectite; P = porous; Py = pyrite.

dissolution pores and cracks constitute almost 2 vol. % of the porosity. The white and the reddish-brown sandstones are partially cemented by smectite rims associated with fine-grained pyrite (Figure 5B). Minor smectite also replaces feldspar grains. In outcrop, bitumen is concentrated in the cross-bedding or as disseminated spots (Figure 4A, B, E) and develops typical dendritic habit toward the finest grained sandstones. In thin sections, bitumen coats the grains and fills fractures and cleavage planes in feldspar and mica (Figure 5A). Late analcite cement locally develops drusiform habit with subhedral and twinned crystals protruding into open spaces. In the reddish-brown facies, pyrite is partially altered to goethite

and hematite, leading to the reddish-brown coloration to the rock (Figures 4D; 5C).

The yellowish-gray and medium-gray facies consist of medium- to coarse-grained sandstone and conglomerate pervasively cemented by multiple calcite generations, which develop a floating grain texture because of the dissolution and replacement of previous cements and grains by calcite (Figure 5D). Both facies display bitumen impregnations, but they are more abundant in the medium-gray facies (Figure 4). Bitumen occurs as disseminated spots in cross-bedding planes, in subhorizontal and discordant tubular and radial pipes and as flames (Figure 4A, G). Two kinds of bitumen were differentiated: (1) a



pervasive brown bitumen with a greasy luster, and (2) a less common massive and black bitumen that cuts the brown bitumen and shows conchoidal fracture. Both types of bitumen coat the grains and fill pores and cracks in the rocks (Figure 5A, D). The SEM images show the typical tension cracks in the bitumen surfaces as a result of the loss of volatile hydrocarbons. In the conglomerates, many clay chips show a yellowish-gray color because of partial replacement by micritic calcite (I) later impregnated by the brown bitumen with dendritic habit (Figure 4). Other clay chips have a grayish-green to grayish-yellow color (5Y7/2 to 5GY8/1; Figure 4) and contain 60–80 vol. % clays, consisting of smectite and subordinate kaolinite.

The yellowish-gray and medium-gray facies host many carbonate concretions (Figure 4A–C, F) formed by multiple stages of calcite crystallization: (1) an early, nonluminescent micritic calcite (I) cements the rocks and also replaces grains, mud chips, and biogenic structures, such as roots, and as *Microcodium* (Kosir, 2004); (2) isopach rims of prismatic calcite (II); (3) coarser grained, cloudy sparry calcite (III, IV 10–100  $\mu\text{m}$ ); and (4) drusiform clear calcite (V) that partially fills open spaces. The calcite (II) and the calcite (III) cements develop oscillatory zoning because of the alternation of dull and bright luminescent areas that become brighter outward (Figure 6A, B). The brightest luminescent zones correlate with the cloudy calcite zones (Figure 6B). Cathodoluminescence

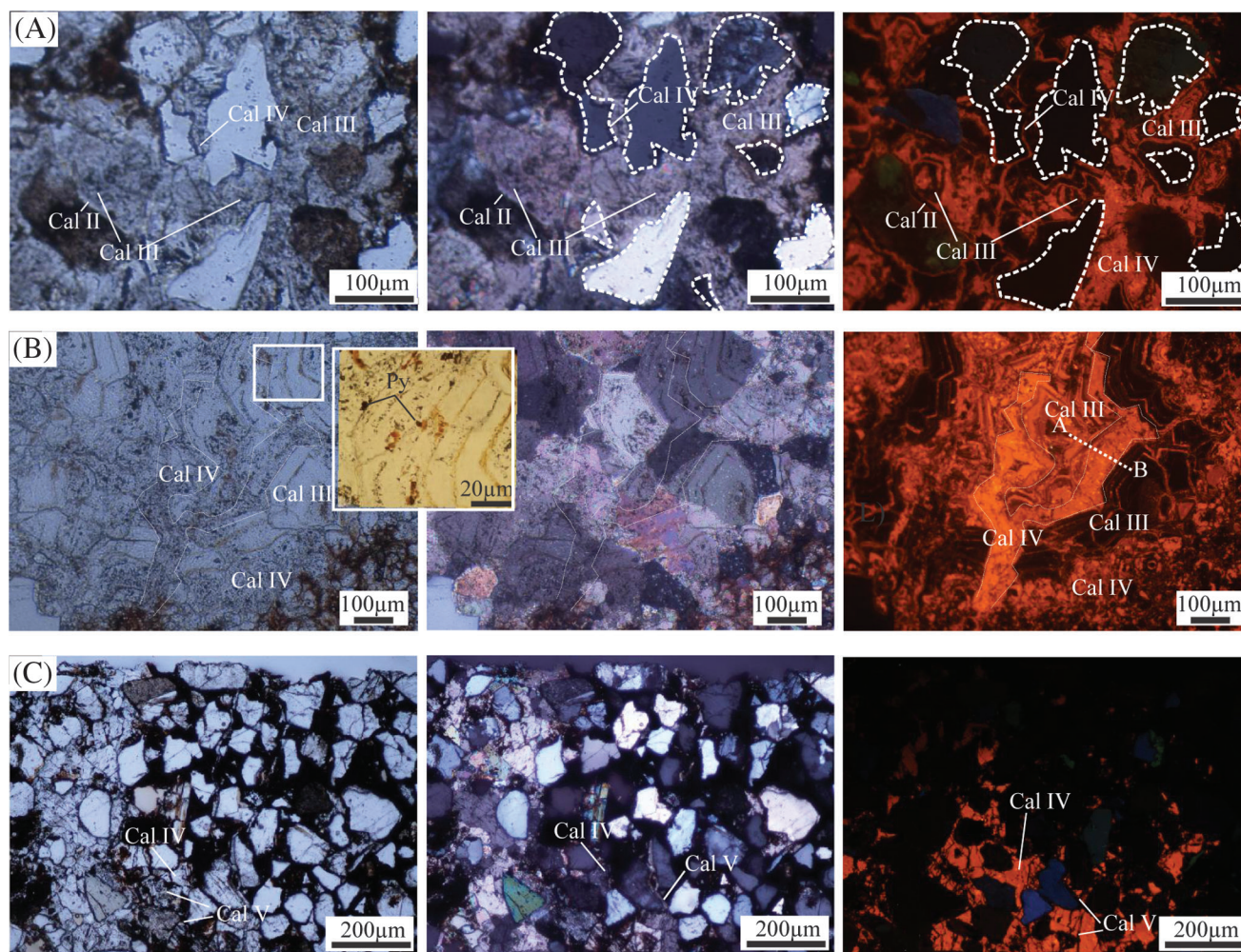


**Figure 6.** (A–C) Photomicrographs of the yellowish- and medium-gray facies showing multiple calcite generations recognized with white light (first two columns from the left) and with cathodoluminescence (third column). See text for further explanation. Cal I, II, III, IV, V = calcite I, II, III, IV, V; Py = pyrite. The white dotted line A–B marks the location of chemical analyses presented in Table 4.

images show evidence of a complex dissolution history for these previous cements and their replacement by patches and veins of homogeneous, syntaxial bright cloudy calcite IV (not visible by optical petrography), resulting in the discontinuity of the isopach calcite rim and complex zoning pattern of calcite III (Figure 6A, B). The cloudy aspect of calcite II, III, and IV is related to the presence of abundant fluid inclusions and many traces of bitumen impregnations that delineate crystal growing sectors (Figure 6B). There are traces of barite cement at the contact with calcites III and IV. The analcite veinlets cut previous cements (Figure 5D) and are surrounded by 60–80  $\mu\text{m}$ -thick microhalos of calcite V. Thin veinlets (15–25  $\mu\text{m}$  [0.59–0.98 thou]) of nonluminescent calcite V cut previous cements in the rock (Figure 6C); this calcite also fills open spaces with typical druse-form habit (Figure 6A) and is frequently associated with gypsum.

### Diagenesis and Alteration of Mudrocks

At Barda González, a pale yellowish-green color dominates in the finest grained facies, preserving the reddish-brown color only in the middle of the thickest mudrock beds. The discoloration starts as disseminated, bleached patches (with bubbles and dendritic shapes) that become much more abundant at the contact with sandstones and conglomerates, tending to form a continuous bleached layer (Figure 4H). The pale yellowish-green color (Figure 4; 5Y7/2) is because of the lack of iron oxide and hydroxide cements and the presence of authigenic smectite and smectite-illite mixed layers (with >70% of smectite) with subordinate kaolinite, fine-grained pyrite/marcasite, and traces of bitumen, calcite and gypsum. The mud chips of the conglomerate layer have a similar composition.

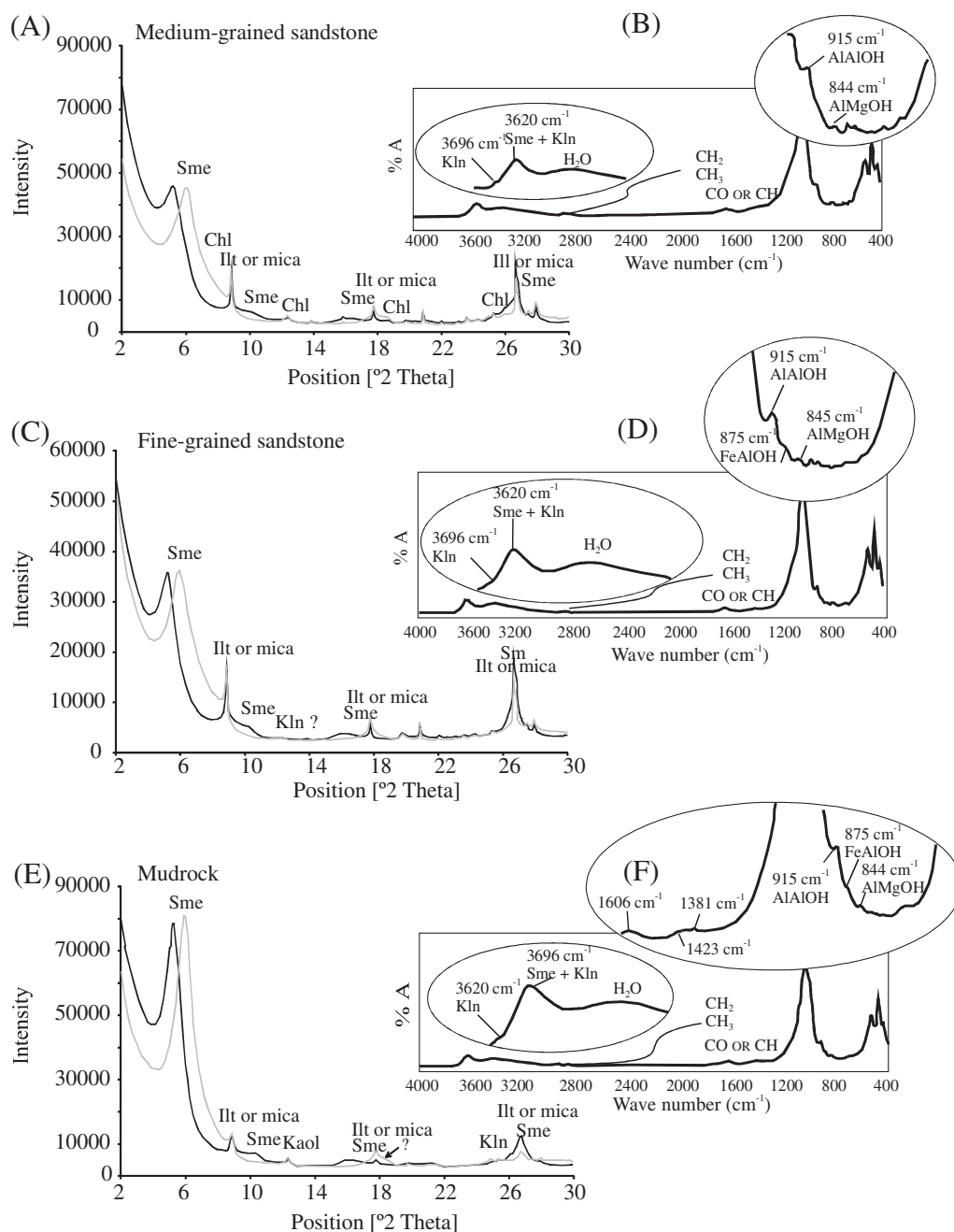
### Composition of Diagenetic Minerals

Clay mineralogies identified by XRD and MIR analyses are shown in figure 7. The MIR spectras of the clay fraction are similar in the bleached sandstones and the mudrocks. The best defined bands belong to minerals of the smectite group (Madejová et al., 2011). The broad band near 3400  $\text{cm}^{-1}$ , a result of OH stretching vibrations of adsorbed water, is characteristic of all

types of smectites. The 3620  $\text{cm}^{-1}$  wide band is representative of the OH stretching of all dioctahedral minerals. The location of the main OH bendings of phyllosilicates into the 800–915  $\text{cm}^{-1}$  domain is also indicative of dioctahedral clay minerals. The 915, 875, and 844  $\text{cm}^{-1}$  bands are due to the bending vibrations of a structural OH in contact with two occupied and one vacant octahedral site. Thus, the bending vibration is a valuable probe of the octahedral sheet in the dioctahedral clay minerals. The 915  $\text{cm}^{-1}$  band is attributed to Al-Al (vacant site) OH bending. At least two components contributed to this band, one from dioctahedral smectite (aluminum-rich smectite) and one from kaolinite (Madejová et al., 2011). However, the XRD data indicate that the contribution of kaolinite is low (Figure 7A, C, E). The 844  $\text{cm}^{-1}$  band is attributed to Al-Mg(OH) bending vibrations. The weak 875  $\text{cm}^{-1}$  band is attributed to Al-Fe<sup>3+</sup>(OH) bending vibrations. Thus, the infrared spectra of the smectite are indicative of a dioctahedral Al-rich smectite with significant Mg substitution in octahedral sites. Such a crystal-chemical characteristic is typical of montmorillonite (i.e., a dioctahedral smectite in which the 2:1 layer charge is mostly a result of R<sup>2+</sup> for Al<sup>3+</sup> substitution in octahedral sites). The bands at 1483–1421  $\text{cm}^{-1}$  region could point to the presence of organic bands (from CO or CH vibrations), and the 2800  $\text{cm}^{-1}$  region is characteristic of traces of aliphatic bonds (CH<sub>2</sub>-CH<sub>3</sub> vibrations).

The chemical microanalysis of the clay cement associated with the bitumen impregnations (Table 2) broadly agrees with that of a montmorillonite in which a significant amount of magnesium (MgO  $\approx$  3%) substitutes to aluminum in octahedral sites (Newman and Brown, 1987). However, they indicate a high but variable amount of iron (3% to 7% of total iron oxide arbitrarily calculated as FeO), which is positively correlated with the deviation of the cation octahedral occupancy toward trioctahedral values in the structural formulas (Table 2). Such a variation of the iron content, which it is not correlated with the variation of the other analyzed major chemical elements (Table 2), is indicative of impurities of nonsilicate iron-bearing minerals in the clay material. This interpretation is corroborated by the low ferric content of the octahedral sites of the smectite indicated

**Figure 7.** (A, C, E) X-ray diffraction patterns for the oriented, non-heated clay fraction (<4 μm) of the medium- to fine-grained sandstones and mudrocks, air-dried (gray line) and after ethylene glycol saturation (black line) and (B, D, F) middle infrared spectra of bleached sandstones and mudrocks. A = absorbance; Chl = chlorite; Ill = illite; Kln = kaolinite; Sme = smectite.



by the infrared spectra (Figure 7B, D, F). According to the petrographic observations, nanoparticles of pyrite seem to be the best candidate as mineral impurity in the smectite cement.

Based on these data, the calculated structural formula can be approximated as follows:  $\text{Ca}_{0.13-0.14} \text{K}_{0.49-0.53} \text{Na}_{0.16-0.21} (\text{Al}_{3-2.75}, \text{Fe}_{0.4-0.97}, \text{Mg}_{0.7-0.83}) (\text{Si}_{7.1-7.44}, \text{Al}_{0.55-0.91}) \text{O}_{20} (\text{OH})_4$ . Such a structural formula approximately fits that of a high-charge montmorillonite (Newman and Brown, 1987).

The XRD analyses and the potassium ferricyanide staining of the yellowish-gray and medium-gray facies indicate that all of the carbonate cements are composed of calcite. Microprobe chemical analyses (Table 3) show differences among the dull (III), bright (IV), and nonluminescent (V) calcites, with an increase in the MnO (0 to 2.41%) and FeO (0 to 0.48%) concentrations from the nonluminescent to the bright calcites. The dull calcite has the highest MgO content (0.03% to 0.59%). The low total oxides



**Table 2.** Representative Microprobe Analyses of Smectite

| Sample  | BG6   |       |       |       |       |       |       |       |       |       |       |       |       |       |       |       |       |       |
|---|-------|-------|-------|-------|-------|-------|-------|-------|-------|-------|-------|-------|-------|-------|-------|-------|-------|-------|
|   | 1     | 2     | 3     | 4     | 5     | 6     | 7     | 8     | 9     | 10    | 11    | 12    | 13    | 14    | 15    | 16    | 17    | 18    |
| (wt.%)  |       |       |       |       |       |       |       |       |       |       |       |       |       |       |       |       |       |       |
| SiO <sub>2</sub>  | 40.91 | 43.90 | 50.72 | 41.50 | 35.96 | 42.44 | 46.38 | 42.91 | 43.12 | 50.57 | 37.98 | 46.26 | 42.71 | 46.23 | 46.12 | 48.10 | 39.37 | 45.06 |
| TiO <sub>2</sub>  | 0.79  | 0.85  | 0.44  | 0.37  | 0.31  | 0.25  | 0.28  | 0.24  | 0.37  | 0.09  | 0.27  | 0.34  | 0.27  | 0.00  | 0.33  | 0.27  | 0.32  | 0.29  |
| Al <sub>2</sub> O <sub>3</sub>                          | 16.40 | 17.46 | 20.55 | 17.79 | 14.12 | 18.60 | 20.50 | 18.81 | 17.45 | 20.94 | 16.41 | 20.02 | 17.79 | 19.78 | 20.86 | 20.44 | 16.16 | 19.61 |
| FeO*  | 4.30  | 3.54  | 4.30  | 4.59  | 5.36  | 6.94  | 6.48  | 5.39  | 4.22  | 3.56  | 3.93  | 5.71  | 3.17  | 5.54  | 4.27  | 3.98  | 3.12  | 3.40  |
| MnO   | 0.05  | 0.02  | 0.00  | 0.01  | 0.00  | 0.10  | 0.06  | 0.10  | 0.00  | 0.04  | 0.06  | 0.07  | 0.05  | 0.04  | 0.01  | 0.00  | 0.03  | 0.07  |
| MgO   | 2.60  | 2.97  | 3.58  | 3.27  | 2.17  | 3.32  | 3.78  | 3.38  | 3.10  | 3.18  | 2.67  | 2.94  | 2.84  | 5.14  | 3.87  | 3.33  | 2.24  | 3.15  |
| CaO   | 0.50  | 1.70  | 0.41  | 1.34  | 0.46  | 0.74  | 0.56  | 0.74  | 0.62  | 0.86  | 0.37  | 0.39  | 1.93  | 0.65  | 0.16  | 1.60  | 0.23  | 0.25  |
| Na <sub>2</sub> O                                       | 0.64  | 0.46  | 1.12  | 0.37  | 0.42  | 0.50  | 0.58  | 0.55  | 0.35  | 0.75  | 0.33  | 0.63  | 0.53  | 0.66  | 0.51  | 0.60  | 0.44  | 0.76  |
| K <sub>2</sub> O  | 2.37  | 2.78  | 2.76  | 2.62  | 2.44  | 2.32  | 2.55  | 2.65  | 2.32  | 2.84  | 2.43  | 2.72  | 2.56  | 1.64  | 2.72  | 3.10  | 2.88  | 2.76  |
| Total   | 68.56 | 73.67 | 83.89 | 71.85 | 61.24 | 75.23 | 81.17 | 74.76 | 71.54 | 82.84 | 64.44 | 79.07 | 71.85 | 79.69 | 78.86 | 81.41 | 64.80 | 75.34 |
| Number of cations for O <sub>20</sub> (OH) <sub>4</sub> |       |       |       |       |       |       |       |       |       |       |       |       |       |       |       |       |       |       |
| <sup>IV</sup> Si  | 7.37  | 7.35  | 7.41  | 7.18  | 7.36  | 7.09  | 7.12  | 7.15  | 7.40  | 7.44  | 7.27  | 7.25  | 7.32  | 7.15  | 7.18  | 7.28  | 7.45  | 7.31  |
| <sup>IV</sup> Al  | 0.63  | 0.65  | 0.59  | 0.82  | 0.64  | 0.91  | 0.88  | 0.85  | 0.60  | 0.56  | 0.73  | 0.75  | 0.68  | 0.85  | 0.82  | 0.72  | 0.55  | 0.69  |
| ∑ <sup>VI</sup>   | 8.00  | 8.00  | 8.00  | 8.00  | 8.00  | 8.00  | 8.00  | 8.00  | 8.00  | 8.00  | 8.00  | 8.00  | 8.00  | 8.00  | 8.00  | 8.00  | 8.00  | 8.00  |
| <sup>VI</sup> Al  | 2.85  | 2.80  | 2.94  | 2.80  | 2.76  | 2.75  | 2.83  | 2.84  | 2.92  | 3.07  | 2.97  | 2.95  | 2.91  | 2.76  | 3.00  | 2.93  | 3.05  | 3.06  |
| Fe  | 0.65  | 0.50  | 0.53  | 0.66  | 0.92  | 0.97  | 0.83  | 0.75  | 0.61  | 0.44  | 0.63  | 0.75  | 0.45  | 0.72  | 0.56  | 0.50  | 0.49  | 0.46  |
| Ti  | 0.11  | 0.11  | 0.05  | 0.05  | 0.05  | 0.03  | 0.03  | 0.03  | 0.05  | 0.01  | 0.04  | 0.04  | 0.04  | 0.00  | 0.04  | 0.03  | 0.05  | 0.04  |
| Mg  | 0.70  | 0.74  | 0.78  | 0.84  | 0.66  | 0.83  | 0.87  | 0.84  | 0.79  | 0.70  | 0.76  | 0.69  | 0.73  | 1.18  | 0.90  | 0.75  | 0.63  | 0.76  |
| Mn  | 0.01  | 0.00  | 0.00  | 0.00  | 0.00  | 0.01  | 0.01  | 0.01  | 0.00  | 0.00  | 0.01  | 0.01  | 0.01  | 0.01  | 0.00  | 0.00  | 0.00  | 0.01  |
| ∑ <sup>VI</sup>   | 4.31  | 4.14  | 4.30  | 4.36  | 4.39  | 4.59  | 4.57  | 4.47  | 4.37  | 4.22  | 4.41  | 4.43  | 4.13  | 4.67  | 4.50  | 4.22  | 4.23  | 4.33  |
| Ca  | 0.10  | 0.30  | 0.06  | 0.25  | 0.10  | 0.13  | 0.09  | 0.13  | 0.11  | 0.14  | 0.08  | 0.07  | 0.35  | 0.11  | 0.03  | 0.26  | 0.05  | 0.04  |
| K   | 0.54  | 0.59  | 0.51  | 0.58  | 0.64  | 0.49  | 0.50  | 0.56  | 0.51  | 0.53  | 0.59  | 0.54  | 0.56  | 0.32  | 0.54  | 0.60  | 0.69  | 0.57  |
| Na  | 0.22  | 0.15  | 0.32  | 0.12  | 0.17  | 0.16  | 0.17  | 0.18  | 0.12  | 0.21  | 0.12  | 0.19  | 0.18  | 0.20  | 0.15  | 0.18  | 0.16  | 0.24  |
| ∑ Interlayer  | 0.86  | 1.05  | 0.90  | 0.95  | 0.90  | 0.79  | 0.76  | 0.87  | 0.74  | 0.88  | 0.79  | 0.80  | 1.09  | 0.63  | 0.72  | 1.03  | 0.90  | 0.85  |

\*All iron as a Fe<sup>2+</sup>.

∑<sup>VI</sup> = sum of octahedral cations.

**Table 3.** Representative Microprobe Analyses of Calcites (III, IV, and V) from Sample BG8078 and Their Behavior Observed under Cathodoluminescence and UV Light\*

| Calcite Type/<br>Oxides W% | CO <sub>2</sub> | MgO   | SiO <sub>2</sub> | CaO    | MnO   | FeO   | CuO   | PbO   | Sum    | Cat.           | UV Light          |
|----------------------------|-----------------|-------|------------------|--------|-------|-------|-------|-------|--------|----------------|-------------------|
| Cal III                    | 43.826          | 0.040 | 0.000            | 55.770 | 0.000 | 0.020 | 0.090 | 0.000 | 99.75  | Dull           | Nonfluorescent    |
| Cal III                    | 43.789          | 0.700 | 0.000            | 54.490 | 0.320 | 0.070 | 0.030 | 0.010 | 99.4   | Dull           | Green fluorescent |
| Cal III                    | 43.972          | 0.340 | 0.000            | 55.390 | 0.210 | 0.010 | 0.010 | 0.000 | 99.94  | Dull           | Green fluorescent |
| Cal III                    | 44.229          | 0.980 | 0.000            | 54.970 | 0.000 | 0.040 | 0.000 | 0.000 | 100.21 | Dull           | Nonfluorescent    |
| Cal IV                     | 42.287          | 0.100 | 0.000            | 51.870 | 1.810 | 0.550 | 0.010 | 0.050 | 96.66  | Bright         | Nonfluorescent    |
| Cal IV                     | 42.946          | 0.100 | 0.000            | 51.970 | 3.110 | 0.210 | 0.020 | 0.000 | 98.36  | Bright         | Nonfluorescent    |
| Cal IV                     | 42.983          | 0.100 | 0.000            | 52.710 | 1.850 | 0.550 | 0.000 | 0.000 | 98.18  | Bright         | Nonfluorescent    |
| Cal IV                     | 42.873          | 0.110 | 0.000            | 52.450 | 1.940 | 0.610 | 0.000 | 0.010 | 97.96  | Bright         | Nonfluorescent    |
| Cal V                      | 44.082          | 0.010 | 0.000            | 56.150 | 0.000 | 0.000 | 0.050 | 0.020 | 100.31 | Nonluminescent | Nonfluorescent    |
| Cal V                      | 44.192          | 0.100 | 0.000            | 56.140 | 0.000 | 0.010 | 0.020 | 0.000 | 100.45 | Nonluminescent | Nonfluorescent    |
| Cal V                      | 44.485          | 0.000 | 0.000            | 56.690 | 0.000 | 0.000 | 0.060 | 0.000 | 101.23 | Nonluminescent | Nonfluorescent    |

\*Cal = calcite; Cat. = cathodoluminescence.

(96.6–98 wt. %) in the analyses of the bright luminescent calcite correlate with zones of high content of fluid inclusions.

### Fluorescence and Fluid Inclusions Studies

In the yellowish- and medium-gray facies, the calcite I does not contain fluid inclusions and shows two distinctive behaviors when observed with ultraviolet (UV) light: (1) the microsparitic calcite has a slightly green fluorescence, and (2) the calcite with *Microcodium* texture does not fluoresce (Figures 8A, B). The nonfluorescent isopach rim of calcite (II) hosts very small (<2 μm) and light-brown fluid inclusions aligned parallel to the clast edges (Figure 8C, D). These fluid inclusions show a weak yellowish-green fluorescence. The calcite III shows a zonation because of the alternation of grayish-green fluorescence and nonfluorescence bands; it hosts primary fluid inclusions (<2–12.5 μm) with yellowish-green fluorescence (Figure 8C–H). The external zone of calcite III crystals and the cloudy, nonluminescent calcite IV host numerous fluid inclusions similar to the baroque carbonate of Tucker et al. (1990) with the following association (Figure 9A–D): (1) regular (triangular shape), one-phase fluid inclusions (type I); (2) irregular to regular, two-phase fluid inclusions (type II); and (3) irregular multiphase fluid inclusions (type III). All types of fluid inclusions

(I, II, and III) are associated with tiny pyrite crystals. Type I fluid inclusions can be subdivided into the following subtypes: (1) moderate relief and light-tan coloration (type Ia), (2) low relief and pinkish hue (type Ib), and (3) high relief and dark-brown color (type Ic). Type I fluid inclusions show a yellowish-green fluorescence in the core of the calcite III crystals and a light-blue fluorescence in the calcite IV (Figures 8H; 9B). Type II fluid inclusions show different behavior under UV light: (1) a group (type IIa) with variable liquid/bubble ratio between 7/3 and 6/4 and a yellowish-green fluorescence low-relief liquid and nonfluorescent high-relief bubble; and (2) a group (type IIb) of triangular and regular shape, very small (≤3 μm), nonfluorescent liquid-rich (9.5/0.5) fluid inclusions with low relief and a tiny pink bubble, mobile at room temperature. The multiphase fluid inclusions show variable behavior under UV light, but frequently some of the liquid phase shows green to light-blue fluorescence. Most of the bitumen (I and II) that impregnates the sandstones does not fluoresce, but in some places, where it coats the grains and fractures or when it is in the contact with quartz grains, it has a yellowish-green, medium to intense fluorescence. Generally, the bitumen is aligned with fluid inclusion (type Ia, b, c, II, and III) trends of similar fluorescence (yellowish-green or blue) cutting the grains (quartz) or along the cleavage surfaces of the feldspars (Figure 9F).

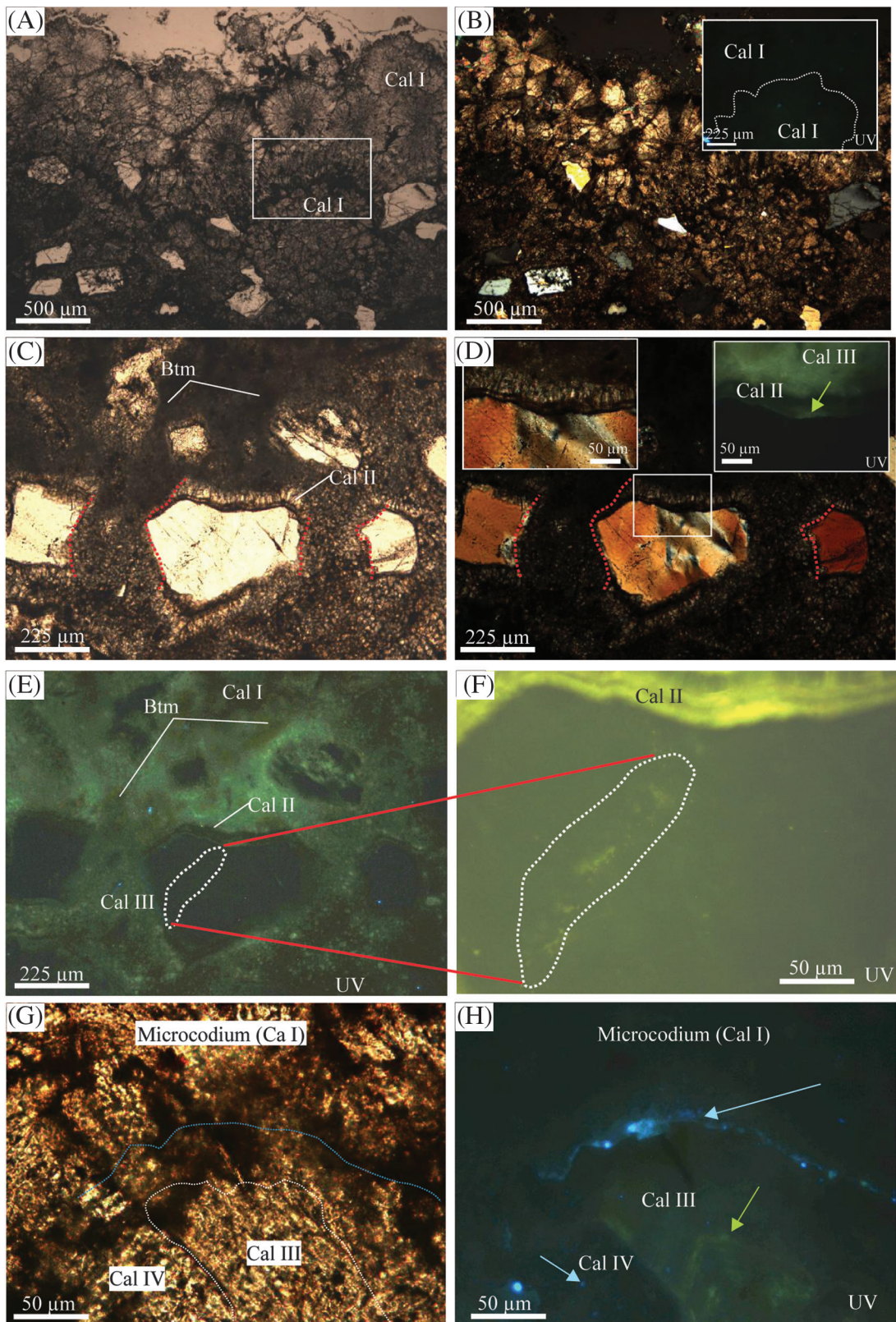


**Figure 8.** (A–H) Photomicrographs of the yellowish- and medium-gray facies showing multiple calcite generations recognized using UV illumination. The light-blue and green arrows point to the organic fluid inclusions with bluish and greenish fluorescence, respectively, hosted in calcite III and IV. Cal = calcite.



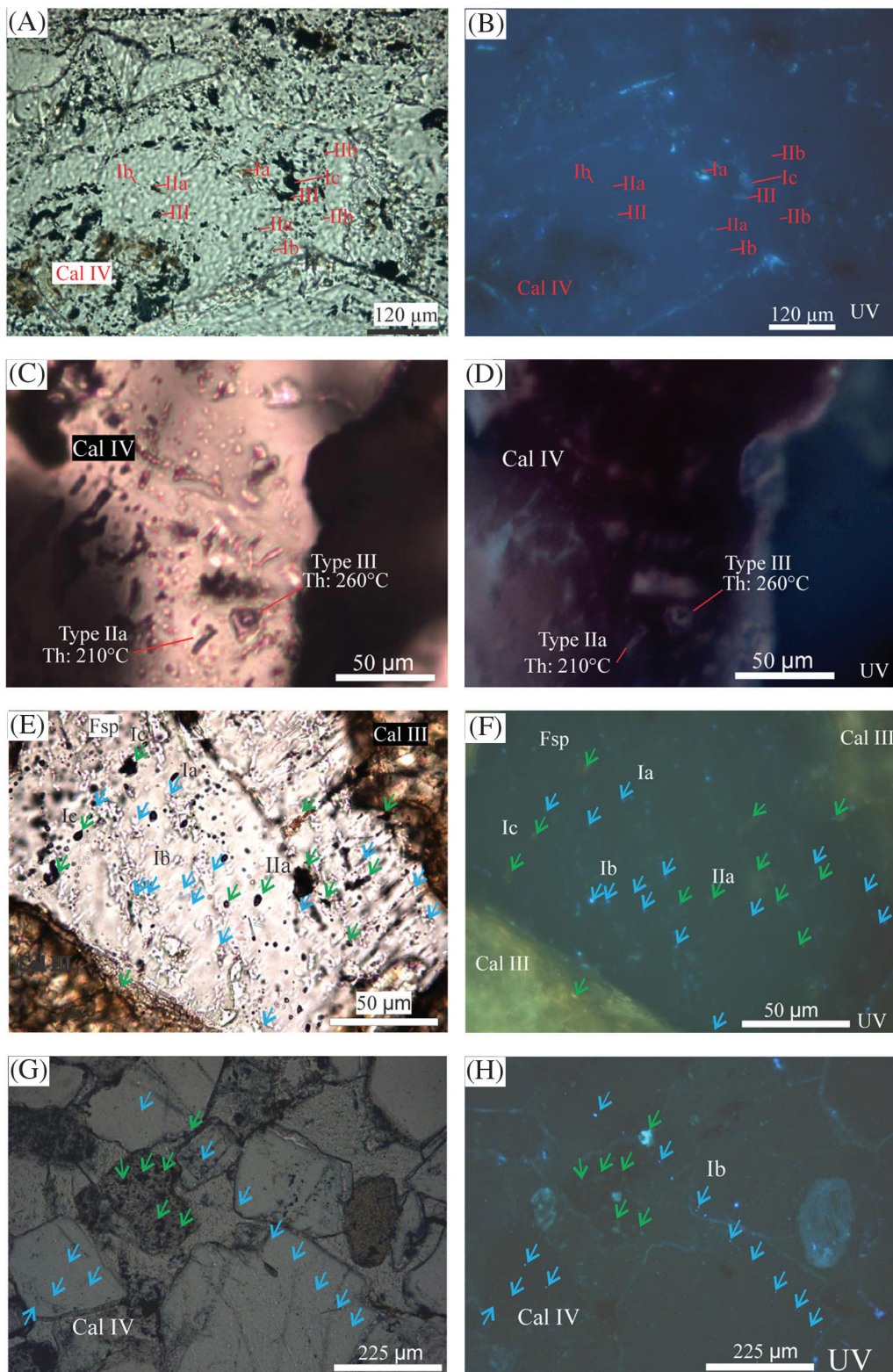


**Figure 9.** Photomicrographs of yellowish- and medium-gray facies show the fluid inclusion assemblages recognized with white and ultraviolet light (UV) (A–D) hosted in the calcite IV and (E–H) hosted as secondary fluid inclusion trends in quartz and feldspar grains. The light-blue and green arrows point to organic fluid inclusions with bluish and greenish fluorescence, respectively. Cal = calcite [III and IV, see text]; Fsp = feldspar; Th = homogenization temperatures of fluid inclusion; Ia, b, IIa, IIb, III, reference the type of fluid inclusion defined in the text.

Preliminary thermometric analyses of aqueous type IIb fluid inclusions hosted in calcite III homogenized to a liquid at 113°C (235°F). The remaining type IIb fluid inclusions hosted in calcite III and IV were too small to be correctly analyzed. The type IIa fluid inclusions (25) show critical temperatures variable between 160–281°C (320°F–538°F) (Figure 8C, D), indicating the presence of organic components (coincident with the critical temperatures of isopentane-isooctane; Levorsen, 1973).

In the white and reddish-brown (sandstone) facies, quartz and feldspar grains host secondary fluid inclusion trends similar to fluid inclusions of calcite

III, calcite IV, and siliciclastic grains of the yellowish- and medium-gray facies (Figure 9E–H).

### Stable Isotope Analyses

In the yellowish-white and medium-gray facies, the  $\delta^{13}\text{C}_{\text{PDB}}$  isotope analyses of calcite III and IV with bright to dull luminescence (Table 4) show a narrow compositional range between  $-8.11\text{‰}$  to  $-8.52\text{‰}$ , and the  $\delta^{18}\text{O}_{\text{PDB}}$  isotopes range from  $-9.76$  to  $-9.87\text{‰}$ . The late, nonluminescent calcite V has the heaviest isotope signature with  $-4.85\text{‰}$   $\delta^{13}\text{C}_{\text{PDB}}$  and  $-7.72\text{‰}$   $\delta^{18}\text{O}_{\text{PDB}}$  values.

**Table 4.** Stable Isotope Compositions of Diagenetic Pyrite/Marcasite and Calcite from the Portezuelo Formation

| Sample   | Depth (m) | Rock     | Mineral | $\delta^{34}\text{S}_{\text{CDT}}$ (‰) |
|----------|-----------|----------|---------|--|
| BG 4325  | 90–91     | Mudstone | Py/Mrc  | –36.4                                  |
| BG 43624 | 87–87     | Mudstone | Mrc     | 18.2                                   |
| BG 43624 | 87–88     | Mudstone | Py      | –24.4                                  |
| BG 43920 | 17–18     | Mudstone | Py      | –60.2                                  |
| BG 46325 | 89–90     | Mudstone | Py      | –59.8                                  |

| Sample   | Rock                    | $\delta^{13}\text{C}_{\text{PDB}}$ (‰) | $\delta^{18}\text{O}_{\text{PDB}}$ (‰) | $\delta^{18}\text{O}_{\text{SMOW}}$ (‰) |
|----------|-------------------------|--|--|---|
| BG0610   | Sandstone (cal-IV)      | –8.23                                  | –8.87                                  | 21.77                                   |
| BG8078-1 | Concretion (cal-III-IV) | –8.11                                  | –9.76                                  | 20.85                                   |
| BG8078-2 | Concretion (cal-III-IV) | –8.52                                  | –9.83                                  | 20.77                                   |
| BG8078-3 | Concretion (cal-V)      | –4.85                                  | –7.72                                  | 22.95                                   |

Cal = calcite; Mrc = marcasite; Py = pyrite.

**Table 5.** (A) Extract and Liquid Chromatography Results, and (B) Gas Chromatography Interpretive Ratios

| (A)      |                    |             |             |          |               |            |
|----------|--------------------|-------------|-------------|----------|---------------|------------|
| Sample   | Total Extract (mg) | Saturated % | Aromatics % | Resins % | Asphaltenes % | Recovery % |
| BG08072c | 8.1                |             |             |          |               |            |
| BG102    | 26.5               | 16.6        | 4.9         | 74       | 1             | 96.6       |

| (B)            |                  |                            |                           |  |  |                         |
|----------------|------------------|----------------------------|---------------------------|--|--|-------------------------|
| Ratios by area | Pristane/Phytane | Pristane/ $n\text{C}_{17}$ | Phytane/ $n\text{C}_{18}$ | $n\text{C}_{18}/(n\text{C}_{18} + n\text{C}_{19})$ | $n\text{C}_{17}/(n\text{C}_{17} + n\text{C}_{27})$ | Carbon preference index |
| BG08072c       | 1.28             | 0.44                       | 0.64                      | 0.54   | 0.88   | 0.96                    |
| BG102          | 1.46             | 0.58                       | 0.9                       | 0.7  | 0.96   | 0.91                    |

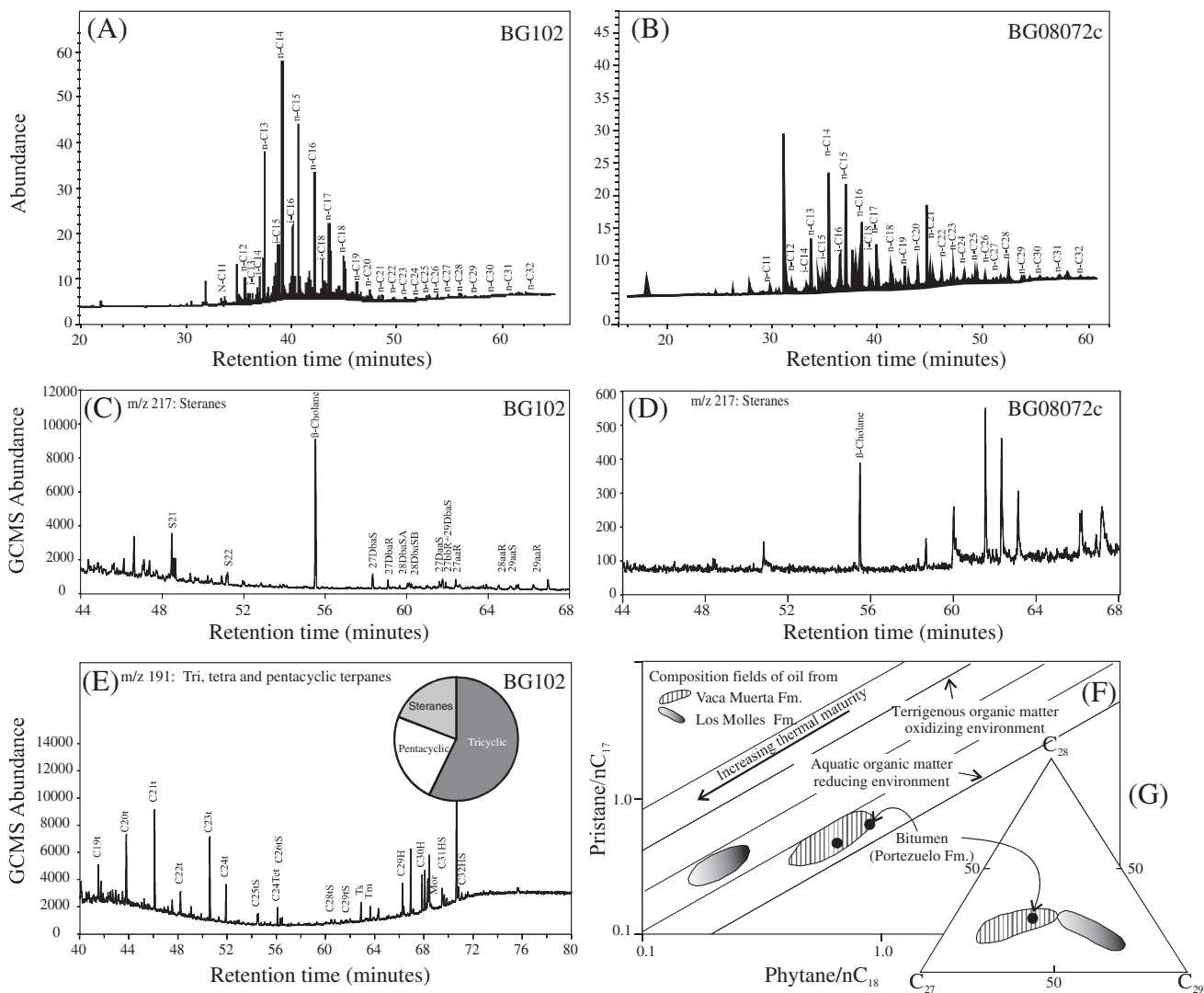
**Table 6.** Chemical Compositions of Formation Water from Aguada Bagüales Oilfield

| Analyses                              | Units                   | QL  | Sample 1058 |
|---------------------------------------|-------------------------|-----|-------------|
| Temperature                           | °C                      |     | 62          |
| pH                                    | pH                      | –   | 6.3         |
| Conductivity                          | microS/cm               | –   | 123800      |
| Total dissolved solids dried at 180°C | mg/l                    | 10  | 92466       |
| Total alkalinity                      | mg CO <sub>3</sub> Ca/l | –   | 524         |
| Chlorides                             | mg/l                    | 5   | 51342       |
| N/NO <sub>2</sub>                     | mg/l                    | 0.1 | <0.1        |
| N/NO <sub>3</sub>                     | mg/l                    | 0.3 | 162.0       |
| Soluble phosphates                    | mg/l                    | 0.2 | 0.6         |
| Sulfates                              | mg/l                    | 5   | 8           |

| Elements (mg/l) | QL    | Metals Dissolved* | Total Metals* |
|-----------------|-------|-------------------|---------------|
| Ag              | 0.021 | <0.084            | <0.210        |
| Al              | 0.06  | 0.35              | <0.60         |
| As              | 0.105 | <0.420            | <1.050        |
| B               | 0.009 | 11.954            | 12.172        |
| Ba              | 0.003 | >200              | 444.572       |
| Ca              | 0.021 | >1000             | 2135.716      |
| Cd              | 0.003 | <0.012            | <0.030        |
| Co              | 0.006 | <0.024            | <0.060        |
| Cr              | 0.012 | <0.048            | <0.120        |
| Cu              | 0.009 | <0.036            | <0.090        |
| Fe              | 0.012 | 0.338             | 19.189        |
| Hg              | 0.03  | <0.12             | <0.30         |
| K               | 0.45  | 495.25            | 512.46        |
| Li              | 0.006 | 32.315            | 33.865        |
| Mg              | 0.06  | 217.99            | 222.46        |
| Mn              | 0.003 | 0.334             | 0.446         |
| Mo              | 0.015 | <0.060            | <0.150        |
| Na              | 0.06  | >2000             | >20000        |
| Ni              | 0.03  | <0.12             | <0.30         |
| P               | 0.15  | <0.60             | <1.50         |
| Pb              | 0.084 | <0.336            | <0.840        |
| Sb              | 0.063 | <0.252            | <0.630        |
| Se              | 0.15  | <0.60             | <1.50         |
| Si              | 0.06  | 11.20             | 14.00         |
| Sn              | 0.051 | <0.204            | <0.510        |
| Sr              | 0.001 | >40               | 395.553       |
| Th              | 0.09  | <0.36             | <0.90         |
| Ti              | 0.006 | <0.024            | <0.060        |
| Tl              | 0.081 | <0.324            | <0.810        |
| U               | 0.45  | <1.80             | <4.50         |
| V               | 0.009 | <0.036            | <0.090        |
| Zn              | 0.006 | <0.024            | <0.060        |

\*The values of dissolved metals and total metals are affected by the dilution factor; QL = quantification limits.



**Figure 10.** Chromatographic analyses of two samples of brown bitumen from the Portezuelo Formation: (A, B) whole extract gas chromatograms; (C, D) steranes; (E) terpanes; (F) the pristane/ $nC_{17}$  versus phytane/ $nC_{18}$  parameters; and (G) sterane biomarker distribution of Portezuelo bitumen and the range of composition of extracts of Vaca Muerta and Los Molles source rocks from the Neuquén Basin for comparison (modified after Cruz et al., 2002). GC = gas chromatography; MS = mass spectrometry.

Stable isotope composition of pyrite/marcasite associated with montmorillonite in the fine-grained facies (mudrocks) show very negative  $\delta^{34}S_{CDT}$  values ( $-24.4$  to  $-60\%$ ) with the exception of one marcasite that shows the most positive  $\delta^{34}S_{CDT}$  value ( $18.2\%$ ) (Table 4).

### Chemical Composition of Bitumen and Subsurface Fluids

The chromatographic analyses of two samples (BG102 and BG08072c) of brown bitumen are shown in Table 5A and Figure 10. Liquid chromatography

results of the sample BG102 indicates that the bitumen in the pores and fractures is rich in resins (Table 5). The migration process would preferentially leave behind the more polar compounds such as resins and asphaltenes. The presence of normal paraffins (straight chain alkanes) indicates that the hydrocarbons in the samples have not been completely biodegraded. The distribution of normal paraffins is dominated by  $C_{14}$  to  $C_{18}$  compounds, indicating that the bitumen was generated by a source unit that reached high thermal maturity near the top of the oil generation window (Figures 10A–F). The higher molecular weight hopanes are low in concentration, but there are



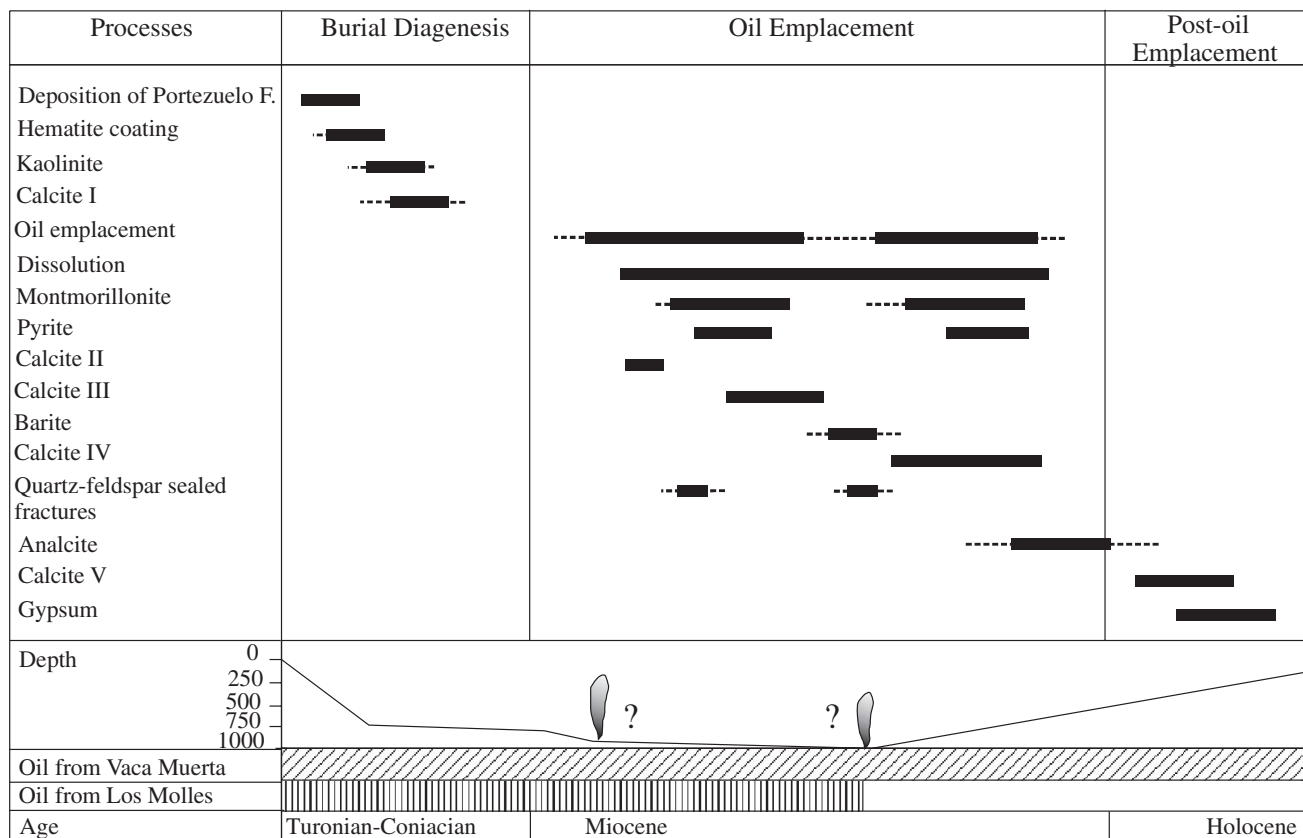


**Figure 11.** Paragenetic sequence and burial history of the Portezuelo Formation with timing of oil generation from the Vaca Muerta and Los Molles source rocks (after Cruz et al., 2002). The Late Cretaceous and Cenozoic deformation of the Neuquén Group (after Schiuma et al., 2002; Silvestro and Zubiri 2008) is interpreted to be contemporaneous with oil emplacement (black flames in the burial diagram) and sandstone alteration.

abundant tri- and tetra-cyclic terpanes, supporting a high maturity for the bitumen (Figures 10C–F). At Aguada Baguales oil field (Figure 3) below Barda González, the hydrocarbons came from 1300 m (4265 ft) below the actual surface (Lotena and Lajas reservoirs). The formation waters that migrated along with the hydrocarbons from these reservoirs rocks show total salinities between 6% to 9% consisting mainly of chlorides with  $\text{Na}^+$ ,  $\text{Ca}^{2+}$ ,  $\text{K}^+$ ,  $\text{Ba}^{2+}$ ,  $\text{Sr}^{2+}$ ,  $\text{Mg}^{2+}$ , and  $\text{Fe}^{2+}$  as soluble cations; they are slightly alkaline ( $\text{pH} \approx 6.5$ ) and their temperature is  $63^\circ\text{C}$  ( $145^\circ\text{F}$ ) (Table 6), the temperature expected at 1300 m (4265 ft) depth in a normal geothermal gradient (Sigismondi and Ramos, 2009).

## DISCUSSION

The nature and arrangement of facies associations observed in the lower and middle sections of the

Portezuelo Formation are similar to those described by Sánchez et al. (2005) for the upper section of the Portezuelo Formation at the Barreales Dam and suggest braided fluvial systems with northeast and northwest paleocurrents. The variations of dominant grain size in the bed load, thickness of channel bodies, and relative proportions of channel/flood plain elements could be a response to long-term fluctuations in discharge levels.

## Diagenesis and Postdating Alteration

In the Dorsal de Huincul region, the Portezuelo Formation reached early diagenesis considering that it was covered by only  $\sim 700$  m (2300 ft) of sediments (Plotier Formation, 102 m [335 ft], Bajo de la Carpa Formation, 75–90 m [245–295 ft], and Anacleto Formation, 65–90 m [213–295 ft] and Malargüe Group, 400 m [1310 ft]; Danderfer and Vera, 1992,

Garrido, 2010; Rodriguez, 2011). Shallow burial of these rocks (Figure 11) suggests that compaction was mainly mechanical, resulting in expulsion of fluids and precipitation of early cements (iron oxides, hydroxides, and calcite I) along with the ductile deformation of mica grains and mud chips. In the fine-grained facies of the Portezuelo Formation, this compaction resulted in escape structures. The proportion of illite (<30%) in the authigenic smectite-illite mixed layers of mudrocks in the Portezuelo Formation is equivalent to the  $R = 0$  of Reichweite ( $R$ ) notation (Reynolds, 1980) and suggests that they formed at shallow depth (Hoffman and Hower, 1979).

The lateral continuity and textural characteristics of the coarse-grained facies in the Portezuelo Formation suggest that they behaved as an aquifer since the early diagenesis. The circulation of low-temperature, oxidizing, and slightly acidic meteoric water could have altered labile minerals to kaolinite and released iron and other trace metals (Walker, 1976; Zielinski et al., 1983; Brown, 2005) that were reprecipitated as amorphous or poorly crystalline iron oxides, which are precursors for hematite (Figure 11; Bjørlykke and Jahren, 2012).

The floating grain texture of the early non-fluorescent calcite (I) cement (Figure 11) and the Microcodium structure indicate formation in a shallow environment (Klappa, 1978; Freytet and Plaziat, 1982; Esteban and Klappa, 1983; Calvet et al., 1991; Kosir, 2004). This carbonate (I) was deposited during early diagenesis in the vadose zone by fluids saturated with  $\text{CO}_3 = + \text{H}_2\text{CO}_3 + \text{HCO}_3^-$  (Scasso and Limarino, 1997) containing abundant  $\text{Ca}^{2+}$  cations in solution. The nonfluorescent behavior of this calcite (I) could be caused by traces (ppm) of  $\text{Fe}^{2+}$  in the mineral lattice, which can act to inhibit fluorescence (Gies, 1975).

Radial isopach calcite (II, Figure 11) implies formation during porous fluid saturation in a phreatic zone (water +  $\text{Ca}^{2+}\text{CO}_3^{2-}$ , Longman, 1980; James and Choquette, 1990). The presence of organic fluid inclusions in calcite rims (II) and sparry calcite (III) (Figures 8H; 9A–D), suggests that oil migration was effective at the time of crystallization (Figure 11). A redox reaction may have been triggered when these hydrocarbons arrived in the sandstones containing

intergranular iron oxide, hydroxide, and carbonate cements. The oxidation of oil during subsurface biodegradation generates  $\text{CO}_2$  and carboxylic acids with a consequent increase in the oil viscosity. Larter et al. (2006) determined that these reactions take place between  $50^\circ$  and  $80^\circ\text{C}$  ( $122^\circ$  and  $176^\circ\text{F}$ ) and at  $\text{pH} \sim 6$ , the range of temperature and  $\text{pH}$  where organic acids reach maximum concentration due to biodegradation. These conditions are similar to those documented for reservoir fluids in the Aguada Baguales oil field (Table 6). Carboxylic acids may have promoted the dissolution of cements from sandstones and conglomerates (Figure 11), evidenced by the floating grain fabric and discontinuity of calcite rims (Figures 6A–B; 8C, D), which may have improved the effective porosity of the rocks and enhanced the permeability. Organic acids may have also contributed to the alteration of labile minerals (feldspar, trioctahedral micas) and their replacement by clay minerals (Bjørkum and Gjeldsvik, 1988; Bjørkum et al., 1993; Bjørlykke et al., 1995; Oelkers and Schott, 1998; Blake and Walter, 1999; Schöner and Gaupp, 2005). The formation of montmorillonite might have occurred locally due to  $\text{pH}/\text{Eh}$  variations that destabilize Al-rich organic complexes by degassing, temperature changes, or mixing with other subsurface water (Surdam et al., 1989). Montmorillonite occluded both primary and secondary porosity of the sandstones.

Microbially mediated reactions of hydrocarbons with diagenetic hematite oxidized hydrocarbons to organic acids, and  $\text{Fe}^{3+}$  was reduced to  $\text{Fe}^{2+}$ . This  $\text{Fe}^{2+}$ , along with available S, precipitated as pyrite accompanying montmorillonite as cement and filling intragrain fractures with hydrocarbons (Figures 5B, C; 11). These reactions resulted in bleaching of the mudrocks and sandstones, the dissolution of iron oxides and hydroxides, and the formation of montmorillonite and pyrite cements. The variable range ( $-60$  to  $18.2\%$ ) and highly negative sulfur isotope values ( $-60$  to  $-24.4\%$ ; Table 3) are characteristic of sulfides generated by microbial sulfate reduction (Seal, 2006). Microbial sulfate reduction accounts for the largest sulfur isotopic fractionations in nature, in some cases, up to  $75\%$  (Wortmann et al., 2001).

In the yellowish- and medium-gray facies cemented by carbonate, the stability of the mineral

facies could be buffered by organic acids that controlled the alkalinity (Willey et al., 1975; Carothers and Kharaka, 1978) and the partial pressure of carbon dioxide ( $P_{CO_2}$ ). Consequently, fluctuations in pH and  $P_{CO_2}$  may be reflected in multiple stages of dissolution and precipitation of calcite (II, III, and IV; Figures 6A, C; 8A, H; James and Choquette, 1990). Quartz and feldspar grains (Figures 10E–H) are cut by multiple trends of fluid inclusions (organic + aqueous) similar to those hosted in calcite II, III, and IV (Figure 9A–D). This suggests that during the precipitation of carbonates, the aqueous fluids were alkaline (pH > 8), dissolved the edges, cleavage planes, and fractures of siliceous clasts and replaced them with calcite (Bennet and Siegel, 1987; Bjørlykke and Egeberg, 1993). In contrast, during the reaction of organic acids with calcite, a decrease in the pH (<8) could cause partial dissolution of calcite (II, III, and IV) and concomitant localized precipitation of quartz and feldspar, sealing the microfractures or cleavage zones, respectively, (Figure 11; Bjørlykke and Egeberg, 1993; Helgeson et al., 1993; Deocampo and Ashley, 1999; Mark et al., 2008) and trapping part of these materials as fluid inclusions (Figure 9E–H). Precipitation of these minerals under these shallow conditions can be explained by the anomalous temperature (70°C [158°F] of reservoir water and 113°C [235°F] measured temperature in fluid inclusion) of hydrocarbons and formation water coming from the deepest reservoir rocks. The presence of abundant fluid inclusions rich in organic fluids (Figures 8H; 9A–D) indicates that during the formation of the carbonates (II–III and IV), the ratio of hydrocarbons to aqueous fluids was high. The variable fluorescence color of the organic fluid inclusions (from yellow in the calcite III to light-bluish in the calcite IV; Figure 8H) indicates that hydrocarbons with different composition interacted with the rocks in the Portezuelo Formation.

The oscillatory zoning observed in calcite II and calcite III (Figure 6A) could be because of changes in the bulk fluid composition ( $aCa^{2+}$ ,  $aMn^{2+}$ , and  $aFe^{2+}$ ), pH/Eh variations, or changes in the crystallization rate during their precipitation (Machel and Burton, 1991). The brightest calcite (III) zones (Figure 6B) are rich in organic fluid inclusions and show the highest  $Mn^{2+}$  and  $Fe^{2+}$  contents (Table 3).

A decrease in the Eh and  $aCa^{2+}$ , along with an increase in  $aMn^{2+}$  and  $aFe^{2+}$ , may have controlled calcite precipitation (Schulman et al., 1947). The grayish-green fluorescent zones of calcite III (Figure 8D) under ultraviolet light can be also attributed to  $Mn^{2+}$  content (Table 2; Gies, 1975; Bissig et al., 2007). The later hydrocarbon charge registered by the fluid inclusions with light-bluish fluorescence may have caused more dissolution of grain minerals and previous cements (calcite I, II, and III; Figure 6A, B) and the precipitation of homogeneous luminescent baroque calcite (IV) with pyrite (Figure 6A, B). Thus, the fluids continued to be saturated with  $Fe^{2+}$ , S,  $Ca^{2+}$ , and  $Mn^{2+}$  (calcite IV; Table 3) during emplacement of the second hydrocarbon charge. The lack of organic fluid inclusions in calcite V and its texture (Figure 6C) indicate that its precipitation postdates hydrocarbon migration.

The bright to dull luminescent calcite II, III, and IV (Figure 6A, B) have more negative  $\delta^{13}C_{PDB}$  and  $\delta^{18}O_{PDB}$  isotope values than the nonluminescent calcite V (Figure 6C; Table 4). Calcite precipitated from the breakdown of hydrocarbons has  $\delta^{13}C_{PDB}$  values as low as  $-20\%$  (Tucker et al., 1990; Wood and Boles, 1991). Therefore, the intermediate  $\delta^{13}C_{PDB}$  compositions observed for calcite II, III, and IV ( $-8.1$  to  $-8.5\%$ ) may have resulted from mixtures of  $^{13}C$ -rich  $CO_2$  derived by dissolution of local calcite with  $^{13}C$ -poor  $CO_2$  derived from oxidizing organic matter (Giuliani et al., 2000). The different  $\delta^{13}C_{PDB}$  values of the latest calcite (V;  $-4.85\%$ ) confirm its precipitation without the direct influence of hydrocarbon fluids.

The abundance of organic fluid inclusions hosted in diagenetic calcites, feldspar, and quartz grains and widespread bitumen impregnations in the sedimentary sequence (Figures 4, 5, 8, 9) indicate that the Portezuelo Formation acted as a carrier bed. The documented slight increase in API gravity from green to blue fluorescence in the organic fluid inclusions (Riecker, 1962; George et al., 2001) could be caused by the following: (1) fluctuation in the groundwater table in the reservoir that resulted in different extents of biodegradation (more intense at the oil water contact [OWC]) or (2) another hydrocarbon pulse having a different evolutionary history (England et al., 1987; Larter et al., 2006).

## Possible Hydrocarbon Source Rocks and Seepage Migration Channels

The chromatographic analysis of the bitumen that impregnates the mineralized sandstones and conglomerates of the Portezuelo Formation indicates large-scale oil migration. These hydrocarbons likely originated from marine organic matter in the Upper Jurassic to Lower Cretaceous Vaca Muerta Formation, the main petroleum source rock in the Dorsal de Huincul (Legarreta et al., 2003, Villar et al., 2005; Figure 10). Hydrocarbons migrated in several stages from this source rock to their traps through carrier beds and faults (Figure 2) from the Early Cretaceous to the Miocene (Cruz et al., 2002; Legarreta et al., 2003). Reactivation of previous Huincul faults from the Cretaceous to the present must have broken the overlying seal rocks (Schiuma et al., 2002; Silvestro and Zubiri, 2008) to produce secondary migration and connection of deep Lajas and Lotena reservoirs with shallow paleochannels of the Neuquén Group (Figure 2A). The presence of solid hydrocarbons in outcrops is clear evidence for this migration.

At local scale, hydrocarbons migrated through the most permeable rocks, following the cross-bedding or the base of the paleochannels (Figure 4). The local traps for these fluids could be (1) vertical and lateral facies changes in the Neuquén Group, like thick mudrock layers in the Cerro Lisandro (69 m [226 ft]) and Plottier Formations (20 m [65.6 ft]; Danderfer and Vera, 1992); and (2) intraformation facies changes, such as the increase in mudrock flood plain facies in the Portezuelo Formation toward the east (Pons et al., 2009). Inside the channels, local changes of permeability resulted in vertical migration, forming cylindrical fluid escape structures (tubes) connecting upward to the most permeable strata. The origin of V-shape flames can be attributed to the dispersion of the hydrocarbons during concomitant groundwater paleoflow.

At the mudrock/sandstone contact, hydrocarbon seepage can be detected by local bleaching of mudrocks, which show bubble and dendriform shapes (Figure 4H). These shapes might have formed by the vertical movement of buoyant light hydrocarbons through a network of interconnected

groundwater-filled microfractures, as described by MacElvain (1969), Price (1986), and Saunders et al. (1999). Similar bleached patterns were observed in the outcrops of the upper Portezuelo Formation section at Barreales Colorado Dam (Giusiano et al., 2009), just above the giant Loma La Lata gas field (Hechem, 2010).

Hydrocarbon migration was accompanied by flow of formation waters having a volume 10 times greater than the volume of hydrocarbons (Surdam et al., 1989). In the study area, the formation waters from the reservoirs are rich in chlorides (5–9%; Table 6, Schiuma et al., 2002; Pons et al., 2009) with Na<sup>+</sup>, Ca<sup>2+</sup>, K<sup>+</sup>, Ba<sup>2+</sup>, Sr<sup>2+</sup>, Mg<sup>2+</sup> and traces of metals in solution. Calcite (II, III, and IV), Mg-montmorillonite, barite, and analcite cements at Barda González may document the infiltration of these brines (Van der Kamp and Leake, 1996). In addition to local sulfate cement, other sources of S to form pyrite could have been enriched sulfate brines coming from dissolution of deep evaporite layers (e.g., Auquilco and Huitrin Formations; Legarreta et al., 1993) and hydrocarbons generated in the Vaca Muerta Formation, which contains sulfur-rich type IIS kerogen (Villar et al., 2005).

## CONCLUSIONS

In the Barda Gonzalez area of the Neuquén Basin, pervasive bleaching of the Portezuelo Formation is evidence that a huge volume of organic fluids circulated through these rocks. The mineralogical signature of the bleaching process is not homogeneous and can be simplified as two main facies: (1) authigenic montmorillonite- and pyrite-cemented facies that correlate with the distribution of medium- to fine-grained sandstones and mudstones, and (2) multi-stages of calcite-pyrite cemented facies coincident with coarse-grained sandstones and conglomerates.

The Neuquén Group represents an important oil and gas reservoir rock in the northern Neuquén Basin (Loma de La Mina, El Sosneado Oriental, Llanquanelo, Loma Alta Sur, and Cerro Fortunoso, El Manzano, Paso de las Bardas Norte, and Valle del Río Grande oil and gas fields; Manacorda et al., 2002; Secretaría de Energía de la Nación, 2014) with cumulative oil



and gas production of 24,769,318 m<sup>3</sup> (155,799,011 barrels) and 52,916,249 m<sup>3</sup> (1,868,716,318 barrels; Secretaría de Energía de la Nación, 2014), respectively. These oilfields are characterized by heterogeneous distributions of porosity (< 5% to 35%) in sandstones and conglomerates (Manacorda et al., 2002) that could be caused by the crystallization of authigenic minerals during different periods of the burial history. This contribution provides for the first time key information to predict the presence of authigenic minerals in the reservoir rocks of the basin, based on the distribution of lithofacies and better understanding of the interaction of organic fluids with red beds of the Portezuelo Formation.

The presence of hydrocarbons in the Neuquén Group shows the connection between the deep reservoir or source rocks and the surface through faults. This fact allows us to propose that Tertiary tectonic events caused failure of the regional seal rocks and favored remigration of oil into shallower units. Our results point to a close relationship between tectonics, hydrocarbon migration, and diagenetic processes in the Dorsal de Huincul region.

## REFERENCES CITED

- Beitler, B., W. T. Parry, and M. A. Chan, 2005, Fingerprints of fluid flow: chemical diagenetic history of the Jurassic Navajo Sandstone, southern Utah, U.S.A.: *Journal of Sedimentary Research*, v. 75, p. 547–561, doi:10.2110/jsr.2005.045.
- Bennet, P., and D. I. Siegel, 1987, Increased solubility of quartz due to complexing by organic compounds: *Nature*, v. 326, p. 684–686, doi:10.1038/326684a0.
- Bissig, T., D. Donosco, N. Guerra, and G. M. Dipple, 2007, Carbonatos en vetas en el distrito epitermal de baja sulfuración de El Peñón, II Región, Chile: ambiente de formación e implicancias para la exploración: *Revista Geológica de Chile*, v. 34, no. 2, p. 291–303.
- Bjørkum, P. A., and N. Gjeldsvik, 1988, An isochemical model for formation of authigenic kaolinite, K-feldspar, and illite in sediments: *Journal of Sedimentary Petrology*, v. 58, p. 506–511.
- Bjørkum, P. A., O. Walderhaug, and N. E. Aase, 1993, A model for the effect of illitization on porosity and quartz cementation of sandstones: *Journal of Sedimentary Petrology*, v. 63, p. 1089–1091, doi:10.2110/jsr.63.1089.
- Bjørlykke, K., P. Aagaard, P. K. Egeberg, and S. P. Simmons, 1995, Geochemical constraints from formation water analyses from the North Sea and the Gulf Coast Basins on quartz, feldspar and illite precipitation in reservoir rocks, in J. M. Cubitt and W. A. England, eds., *The geochemistry of reservoirs: Geochemical Society Special Publication*, v. 86, p. 33–50.
- Bjørlykke, K., and P. K. Egeberg, 1993, Quartz cementation in sedimentary basins: *AAPG Bulletin*, v. 77, p. 1538–1548.
- Bjørlykke, K., and J. Jahren, 2012, Open or closed geochemical systems during diagenesis in sedimentary basins: Constraints on mass transfer during diagenesis and the prediction of porosity in sandstone and carbonate reservoirs: *AAPG Bulletin*, v. 96, p. 2193–2214, doi:10.1306/04301211139.
- Blake, R. E., and L. M. Walter, 1999, Kinetics of feldspar and quartz dissolution at 70–80°C and near-neutral pH: Effects of organic acids and NaCl: *Geochimica et Cosmochimica Acta*, v. 63, p. 2043–2059, doi:10.1016/S0016-7037(99)00072-1.
- Britton, D. R., 1998, The diagenetic effects of hydrocarbon saturation in sandstones of the Green River Formation, Uinta Basin, Utah: Ph.D. thesis, University of Wyoming, Laramie, 165 p.
- Brown, A. C., 2005, Refinements for footwall red-bed diagenesis in the sediment hosted stratiform copper deposits model: *Economic Geology*, v. 100, p. 765–771.
- Calvet, F., V. P. Wright, and J. Giménez, 1991, Microcodium: descripción y origen. Implicaciones paleogeográficas y paleogeomorfológicas: Grupo Español del Terciario, Comunicaciones I Congreso, Vic., p. 50–51.
- Carothers, W. W., and Y. K. Kharaka, 1978, Aliphatic acid anions in oil-field water—Implications for origin of natural gas: *AAPG Bulletin*, v. 62, p. 2441–2453.
- Cazau, L., and M. Uliana, 1972, El Cretácico Superior continental de la Cuenca Neuquina: 5° Congreso Geológico Argentino, Buenos Aires, Actas 3, p. 131–163.
- Chan, M. A., W. T. Parry, and J. R. Bowman, 2000, Diagenetic hematite and manganese oxides and fault-related fluid flow in Jurassic sandstones, southeastern Utah: *AAPG Bulletin*, v. 84, p. 1281–1310.
- Coleman, M. L., and M. P. Moore, 1978, Direct reduction of sulfates to sulfur dioxide for isotopic analysis: *Analytical Chemistry*, v. 50, p. 1594–1595, doi:10.1021/ac50033a056.
- Cruz, C., A. Boll, R. Gómez Omil, E. Martínez, C. Arregui, C. Gulisano, G. Laffitte, and H. Villar, 2002, Hábitat de hidrocarburos y sistemas de carga Los Molles y Vaca Muerta en el sector central de la Cuenca Neuquina, Argentina: 5° Congreso de Exploración y Desarrollo de Hidrocarburos, Mar del Plata, 20 p. CD-ROM.
- Danderfer, J. C., and P. Vera, 1992, Geología, Carta geológica y recursos minerales del Departamento Confluencia, escala 1:200.000, Provincia de Neuquén, República Argentina: Ministerio de la Producción Dirección Provincial de Minería, Servicio Geológico Neuquino, Zapala, Boletín 1, p. 23–45.
- Deocampo, D. M., and G. M. Ashley, 1999, Siliceous islands in a carbonate sea: modern and Pleistocene spring-fed wetlands in Ngorongoro crater and Oldupai Gorge, Tanzania: *Journal of Sedimentary Research*, v. 69, no. 5, p. 974–979, doi:10.2110/jsr.69.974.
- Dickinson, W. R., 1970, Interpreting detrital modes of greywacke and arkose: *Journal of Sedimentary Petrology*, v. 40, p. 695–707.

- Digregorio, R. E., C. A. Gulisano, A. R. Gutiérrez Pleimling, and S. A. Minitti, 1984, Esquema de la evolución geodinámica de la Cuenca Neuquina y sus implicancias paleogeográficas: 9° Congreso Geológico Argentino, San Carlos de Bariloche, v. 2, p. 147–162.
- England, W. A., A. S. Mackenzie, D. M. Mann, and T. M. Quigley, 1987, The movement and entrapment of petroleum fluids in the subsurface: *Journal of the Geological Society, London*, v. 144, p. 327–347, doi:10.1144/gsjgs.144.2.0327.
- Esteban, M., and C. F. Klappa, 1983, Subaerial exposure environment, in P. A. Scholle, D. G. Bebout, and C. H. Moore, eds., *Carbonate Depositional Environments: AAPG Memoir 33*, p. 1–54.
- Folk, R. L., P. B. Andrews, and D. W. Lewis, 1970, Detrital sedimentary rock classification and nomenclature for use in New Zealand: *Journal of Geology and Geophysics*, v. 13, p. 937–968, doi:10.1080/00288306.1970.10418211.
- Foxford, K. A., I. R. Garden, S. C. Guscott, S. D. Burley, J. J. M. Lewis, J. J. Walsh, and J. Waterson, 1996, The field geology of the Moab fault, in A. C. Huffman, Jr., W. R. Lund, and I. H. Goodwin, eds., *Geology and resources of the Paradox Basin: Utah Geological Association, Guidebook 25*, p. 265–283.
- Franzese, J., L. A. Spalletti, I. G. Perez, and D. Macdonald, 2003, Tectonic and paleoenvironmental evolution of Mesozoic sedimentary basins along the Andean foothills of Argentina (32°–54°S): *Journal of South American Earth Sciences*, v. 16, p. 81–90, doi:10.1016/S0895-9811(03)00020-8.
- Freytet, P., and J. C. Plaziat, 1982, Continental carbonate sedimentation and pedogenesis-Late Cretaceous and early Tertiary of southern France: Stuttgart, Schweitzerbart'sche Verlagsbuchhandlung: *Contributions to Sedimentology*, v. 12, 213 p.
- Garden, I. R., S. C. Guscott, S. D. Burley, K. A. Foxford, J. J. Walsh, and J. Marshall, 2001, An exhumed paleohydrocarbon migration fairway in a faulted carrier system, Entrada Sandstone of southeastern Utah, U.S.A.: *Geofluids*, v. 1, p. 195–213, doi:10.1046/j.1468-8123.2001.00018.x.
- Garrido, A. C., 2010, Estratigrafía del Grupo Neuquén, Cretácico Superior de la Cuenca Neuquina (Argentina): nueva propuesta de ordenamiento litoestratigráfico: *Revista del Museo Argentino de Ciencias Naturales*, v. 12, no. 2, p. 121–177.
- Gazzi, P., 1966, Le arenarie del flysch sopracretaceo dell'Appennino modenese; correlazioni con il flysch di Monghidoro: *Miner. Petrogr. Acta*, v. 12, p. 69–97.
- George, S. C., T. E. Ruble, A. Dutkiewicz, and P. J. Eadington, 2001, Assessing the maturity of oil trapped in fluid inclusions using molecular geochemistry data and visually-determined fluorescence colours: *Applied Geochemistry*, v. 16, p. 451–473, doi:10.1016/S0883-2927(00)00051-2.
- Gies, H. 1975, Activation possibilities and geochemical correlations of photoluminescing carbonates, particularly calcites: *Mineralium Deposita*, v. 10, p. 216–227, doi:10.1007/BF00207138.
- Giuliani, G., C. France-Lanord, A. Cheillietz, P. Coget, Y. Branquet, and B. Laumonnier, 2000, Sulfate reduction by organic matter in colombian emerald deposits: Chemical and stable isotope (C, O, H) evidence: *Economic Geology*, v. 95, p. 1129–1153.
- Giusiano, A., and E. Bouhier, 2009, Mineralización de Cu en el Grupo Neuquén vinculada a la migración de hidrocarburos. Dorso de los Chihuidos, Neuquén, Argentina: *Boletín de Informaciones Petroleras*, v. 11, p. 6–18.
- Giusiano, A., M. Franchini, A. Impiccini, and M. S. O'Leary, 2006, Mineralización de Cu asociada a bitumen en las areniscas cretácicas, Prospecto Barda González, Neuquén, Argentina: 11° Congreso Geológico Chileno, v. 2, p. 255–258.
- Giusiano, A., M. Franchini, A. Impiccini, and M. J. Pons, 2008, Mineralización de Cu en sedimentitas Mesozóicas del Grupo Neuquén y hábitat de los hidrocarburos en la Dorsal de Huincul Neuquén (abs.): 17° Congreso Geológico Argentino, Simposio de la Cuenca Neuquina, San Salvador de Jujuy, p. 769–770.
- Giusiano, A., M. B. Franchini, M. J. Pons, and A. Impiccini, 2009, Mineralización de Cu en el Grupo Neuquén asociada a la presencia de hidrocarburos, Dorsal de Huincul, Neuquén, Argentina (abs.): 9° Congreso Argentino de Geología Económica, San Fernando del Valle de Catamarca, p. 11.
- González, P. D., M. F. Tortello, and S. E. Damborenea, 2011, Early Cambrian archaeocyathan limestone blocks in low-grade meta-conglomerate from El Jagüelito Formation (Sierra Grande, Río Negro, Argentina): *Geológica Acta*, v. 9, no. 2, p. 159–163.
- Gulisano, C. A., A. R. Gutiérrez Pleimling, and R. E. Digregorio, 1984, Análisis estratigráfico del intervalo Tithoniano–Valanginiano (Formaciones Vaca Muerta, Quintuco y Mulichinco) en el suroeste de la provincia de Neuquén: 9° Congreso Geológico Argentino, San Carlos de Bariloche, p. 221–235.
- Hair, A., J. Hladikova, and V. Smejkal, 1973, Procedure of direct conversion of sulfates into SO<sub>2</sub> for mass spectrometric analysis of sulfur: *Isotope Praxis*, v. 18, p. 433–436.
- Hechem, J. J., 2010, Breve historia sobre el descubrimiento de Loma La Lata: *Petrotecnia revista del Instituto Argentino del Petróleo y Gas*, v. 2, p. 11–17.
- Helgeson, H. G., A. M. Knox, C. E. Owens, and E. L. Shock, 1993, Petroleum, oil field water, and authigenic assemblages: Are they in metastable equilibrium in hydrocarbon reservoir?: *Geochimica et Cosmochimica Acta*, v. 57, p. 3295–3339.
- Hoffman, J., and J. Hower, 1979, Clay mineral assemblages as low grade metamorphic geothermometers: Application to the thrust faulted disturbed belt of Montana, in P. A. Scholle and P. S. Schluger, eds., *Aspects of diagenesis: SEPM Special Publication 26*, p. 55–79.
- Holt, B. D., and A. G. Engelkemeier, 1970, Thermal decomposition of barium sulfate to sulfur dioxide for mass spectrometric analysis: *Analytical Chemistry*, v. 42, p. 1451–1453, doi:10.1021/ac60294a032.

- Ingersoll, R. V., T. F. Fullard, R. L. Ford, J. P. Grimm, J. D. Pickle, and S. W. Sares, 1984, The effect of grain size on detrital modes: a test of the Gazzi–Dickinson point-counting method: *Journal of Sedimentary Research*, v. 54, p. 103–116.
- James, N. P., and P. W. Choquette, 1990, Limestone the meteoric diagenetic environment, in I. A. McIlreath and D. W. Morrow, eds., *Diagenesis: Geoscience Canada*, 11, p. 161–164.
- Klappa, C. F., 1978, Biolithogenesis of Microcodium: elucidation: *Sedimentology*, v. 25, p. 489–522, doi:[10.1111/sed.1978.25.issue-4](https://doi.org/10.1111/sed.1978.25.issue-4).
- Kosir, A., 2004, Microcodium revisited: root calcification products of terrestrial plants on carbonate rich substrates: *Journal of Sedimentary Research*, v. 74, p. 845–857, doi:[10.1306/040404740845](https://doi.org/10.1306/040404740845).
- Larter, S., H. Huang, J. Adams, B. Bennett, O. Jokanola, T. Oldenburg, M. Jones, I. Head, C. Riediger, and M. Fowler, 2006, The controls on the composition of biodegraded oils in the deep subsurface: Part II—Geological controls on subsurface biodegradation fluxes and constraints on reservoir–fluid property prediction: *AAPG Bulletin*, v. 90, p. 921–938, doi:[10.1306/01270605130](https://doi.org/10.1306/01270605130).
- Leanza, H., S. Apestegua, F. E. Novas, and M. S. De la Fuente, 2004, Cretaceous terrestrial beds from the Neuquén Basin (Argentina) and their tetrapod assemblages: *Cretaceous Research*, v. 25, p. 61–87, doi:[10.1016/j.cretres.2003.10.005](https://doi.org/10.1016/j.cretres.2003.10.005).
- Legarreta, L., and C. A. Gulisano, 1989, Análisis estratigráfico de la Cuenca Neuquina (Triásico superior–Terciario inferior), Argentina, in G. Chebli and L. A. Spalletti, eds., *Cuencas Sedimentarias Argentinas: Facultad de Ciencias Naturales, Universidad Nacional de Tucumán, Serie Correlación Geológica*, v. 6, p. 221–243.
- Legarreta, L., C. A. Gulisano, and M. A. Uliana, 1993, Las secuencias Sedimentarias Jurásico–Cretácicas, in V. A. Ramos, ed., *Geología y Recursos Naturales de Mendoza: Relatorio del 12° Congreso Geológico Argentino*, Mendoza, p. 87–114.
- Legarreta, L., and M. A. Uliana, 1991, Jurassic–Cretaceous marine oscillations and geometry of backarc basin fill, Central Argentine Andes, in D. I. Macdonald, ed., *Sedimentation, Tectonics and Eustasy: Sea level Changes at Active Plate Margins: International Association of Sedimentologists Special Publication 12*, p. 429–450.
- Legarreta, L., and M. A. Uliana, 1996a, La sucesión Jurásica en el centro-oeste de Argentina. Arreglo estratigráfico, secuencias y evolución paleogeográfica: *Boletín de Informaciones Petroleras*, v. 45, p. 66–78.
- Legarreta, L., and M. A. Uliana, 1996b, The Jurassic succession in westcentral Argentina: stratal patterns, sequences and paleogeographic evolution: *Palaeogeography, Palaeoclimatology and Palaeoecology*, v. 120, p. 303–330, doi:[10.1016/0031-0182\(95\)00042-9](https://doi.org/10.1016/0031-0182(95)00042-9).
- Legarreta, L., and M. A. Uliana, 1998, Anatomy of hinterland depositional sequences: Upper Cretaceous, fluvial strata, Neuquen Basin, west-central Argentina: Relative role of eustasy in continental rocks: *SEPM Special Publication 59*, p. 83–92.
- Legarreta, L., C. Cruz, G. Vergani, G. Laffitte, and H. Villar, 2003, Source rocks, reserves and resources in the Neuquén Basin, Argentina: Mass balance approach and exploratory potential: *AAPG Bulletin*, v. 87, p. 1–10.
- Levandowski, D. W., M. E. Kaley, and S. R. Silverman, 1973, Cementation in Lyons sandstone Colorado: *AAPG Bulletin*, v. 57, p. 2217–2244.
- Levorsen, A. I., 1973, *Geología del Petróleo: Buenos Aires Editorial Universitaria*, 452 p.
- Longman, M. W., 1980, Carbonate diagenetic textures from near shore diagenetic environments: *AAPG Bulletin*, v. 64, p. 461–487.
- Macellari, C. E., 1988, Cretaceous paleogeography and depositional cycles of western South America: *Journal of South American Earth Sciences*, v. 1, p. 373–418, doi:[10.1016/0895-9811\(88\)90024-7](https://doi.org/10.1016/0895-9811(88)90024-7).
- MacElvain, R., 1969, Mechanics of gaseous ascension through a sedimentary column, in W. B. Heroy, ed., *Unconventional methods in exploration for petroleum and natural gas: Dallas, Southern Methodist University Press*, p. 15–28.
- Machel, H. G., and E. A. Burton, 1991, Factor governing cathodoluminescence in calcite and dolomite, and their implications for studies of carbonate diagenesis, in C. E. Barker and O. C. Kopp, eds., *Luminescence Microscopy: Quantitative and Qualitative Aspects: SEPM*, p. 37–57.
- Madejová, J., E. Balan, and S. Petit, 2011, Application of vibrational spectroscopy to the characterization of phyllosilicates and other industrial minerals: *EMU Notes in Mineralogy*, v. 9, Chapter 6, p. 171–226.
- Manacorda, L., S. M. E. Reinante, L. Cazau, and E. Penna, 2002, Los reservorios del Grupo Neuquén, in M. Schiuma, G. Hinterwimmer, and G. Vergani, eds., *Rocas Reservorios de las Cuencas Productivas de la Argentina: 5° Congreso de Exploración y Desarrollo de Hidrocarburos, Mar del Plata*, p. 529–558.
- Mark, D. F., F. P. Green, J. Parnell, S. P. Kelley, M. R. Lee, and S. C. Sherlock, 2008, Late Palaeozoic hydrocarbon migration through the Clair field, West of Shetland, UK Atlantic margin: *Geochimica et Cosmochimica Acta*, v. 72, p. 2510–2533, doi:[10.1016/j.gca.2007.11.037](https://doi.org/10.1016/j.gca.2007.11.037).
- McCrea, J. M., 1950, On the isotopic chemistry of carbonates and a paleotemperature scale: *Journal of Chemical Physics*, v. 18, p. 849–857, doi:[10.1063/1.1747785](https://doi.org/10.1063/1.1747785).
- Miall, A., 1996, *The geology of fluvial deposits: New York, Springer*, 582 p.
- Moore, D. M., and R. J. R. Reynolds, 1997, *X-ray diffraction and the identification and analysis of 593 clay minerals: New York, Oxford University Press*, 378 p.
- Mosquera, A., and V. Ramos, 2006, Intraplate deformation in the Neuquén Embayment, in S. Kay and V. Ramos, eds., *Evolution of an Andean margin: A tectonic and magmatic view from the Andes to the Neuquén Basin (35°–39° latitude): Geological Society of America, Special Paper 407*, p. 97–123.
- Moulton, G. F., 1926, Some features of red bed bleaching: *AAPG Bulletin*, v. 10, p. 304–311.
- Newman, A., and G. Brown, 1987, The chemical constitution of clays, in A. Newman, ed., *Chemistry of Clays and*

- Clay Minerals: Mineralogical Society Monograph, no. 6, p. 1–129.
- Oelkers, E. H., and J. Schott, 1998, Does organic acid adsorption affect alkali-feldspar dissolution rates?: *Chemical Geology*, v. 151, p. 235–245, doi:[10.1016/S0009-2541\(98\)00082-5](https://doi.org/10.1016/S0009-2541(98)00082-5).
- Parnell, J., and P. F. Carey, 1995, Emplacement of bitumen (asphaltite) veins in the Neuquén Basin, Argentina: *AAPG Bulletin*, v. 79, p. 1798–1816.
- Ploszkiewicz, V., L. Orchuela, J. Vaillard, and R. Viñes, 1984, Compresión y desplazamiento lateral en la zona de falla Huincul, estructuras asociadas, Provincia de Neuquén: 9° Congreso Geológico Argentino, Bariloche, Actas 2, p. 163–169.
- Pons, M. J., M. B. Franchini, A. Giusiano, A. Impiccini, and M. Godeas, 2009, Alteraciones, mineralización de Cu y Bitumen en areniscas Cretácicas del Prospecto Barda González, Neuquén, Argentina: *Revista de la Asociación Geológica Argentina*, v. 64, no 3, p. 321–333.
- Pons, M. J., A. Giusiano, M. Franchini, A. Impiccini, J. F. Ríos, and A. Testi, 2011, Diagénesis, alteración y mineralización de Cu en la Formación Huincul, Prospecto Tordillos, Cuenca Neuquina (abs.): 18° Congreso Geológico Argentino, Neuquén, 2 p.
- Price, L. C., 1986, A critical review and proposed working model of surface geochemical exploration, *in* M. J. Davidson, ed., *Unconventional methods in exploration for petroleum and natural gas IV*: Dallas, Southern Methodist University Press, p. 245–304.
- Rainoldi, A. L., M. Franchini, D. Beaufort, P. Patrier, A. Giusiano, A. Impiccini, and M. J. Pons, 2014, Large scale bleaching of red beds related to upward migration of hydrocarbons: Los Chihuidos High, Neuquén Basin, Argentina: *Journal of Sedimentary Research*, v. 84, p. 373–393, doi:[10.2110/jsr.2014.31](https://doi.org/10.2110/jsr.2014.31).
- Rainoldi, A. L., M. B. Franchini, N. Cesaretti, A. Impiccini, and M. J. Pons, 2012, Alteración y decoloración de areniscas rojas, Formación Huincul (Grupo Neuquén). Evidencias de la circulación de hidrocarburos en el Dorso de los Chihuidos (abs.): Reunión Argentina de Sedimentología, Salta, p. 183–184.
- Ramos, V. A., 1981, Descripción Geológica de la Hoja 33c, Los Chihuidos Norte. Provincia del Neuquén: Servicio Geológico Nacional, Buenos Aires, Boletín no. 182, p. 1–103.
- Ramos, V. A., 1999, Evolución tectónica de la Argentina, *in* R. Caminos, ed., *Geología Argentina: Instituto de Geología y Recursos Minerales, Anales 29*, no. 24, p. 715–784.
- Ramos, V., and A. Folguera, 2005, Tectonic evolution of the Andes of Neuquén: constraints derived from de magmatic arc and foreland deformation, *in* G. D. Veiga, L. A. Spalletti, J. A. Howell, and E. Schwarz, eds., *The Neuquén Basin, Argentina: A case study in sequence stratigraphy and basin dynamics*: Geological Society, London, Special Publication 252, p. 25–35.
- Ramos, V. A., A. C. Ricardi, and E. O. Roller, 2004, Límites Naturales del Norte de la Patagonia: *Revista de la Asociación Geológica Argentina*, v. 59, no. 4, p. 785–786.
- Reynolds, R. C., 1980, Interstratified clay minerals, *in* G. W. Brindley and G. Brown, eds., *Crystal structures of the clay minerals and their X-ray identification*: London, Mineralogical Society, p. 249–303.
- Riecker, R. E., 1962, Hydrocarbon fluorescence and migration of petroleum: *AAPG Bulletin*, v. 46, p. 60–75.
- Rodríguez, M. F., 2011, El Grupo Malargüe (Cretácico Tardío-Paleógeno Temprano) en la cuenca Neuquina, *in* H. A. Leanza, C. Arregui, O. Carbone, J. C. Danieli, and J. Vallés, eds., *Geología y Recursos Naturales de la Provincia del Neuquén: Relatorio del 18° Congreso Geológico Argentino*, Neuquén, p. 245–263.
- Sánchez, M. L., J. O. Calvo, and S. Heredia, 2005, Paleoambientes de sedimentación del tramo superior de la Formación Portezuelo, Grupo Neuquén (Cretácico Superior), Los Barreales, provincia del Neuquén: *Revista de la Asociación Geológica Argentina*, v. 60, no. 1, p. 142–158.
- Sanford, R. F., 1995, Ground-water flow and migration of hydrocarbons to the Lower Permian White Rim Sandstone, Tar Sand Triangle, southeastern Utah: *U.S. Geological Survey Bulletin* 2000-J, 24 p.
- Saunders, D. F., K. R. Burson, and C. K. Thompson, 1999, Model for hydrocarbon microseepage and related near-surface alterations: *AAPG Bulletin*, v. 83, p. 170–185.
- Scasso, R. A., and C. O. Limarino, 1997, Petrología y diagénesis de rocas clásticas: *Asociación Argentina de Sedimentología, Special Publication 1*, 258 p.
- Schioma, M., C. Saavedra, P. Malone, M. Cevallos, L. Rebori, and G. Vergani 2002, Los reservorios del Gupo Lotena. Argentina, *in* M. Schioma, G. Hinterwimmer, and G. Vergani, eds., *Rocas Reservorios de las Cuencas Productivas de la Argentina, Cuenca Neuquina, Grupo Lotena: 5° Congreso de Exploración y Desarrollo de Hidrocarburos, Mar del Plata*, p. 303–334.
- Schöner, R., and R. Gaupp, 2005, Contrasting red bed diagenesis: the southern and northern margin of the Central European Basin: *International Journal of Earth Sciences*, v. 94, p. 897–916, doi:[10.1007/s00531-005-0004-3](https://doi.org/10.1007/s00531-005-0004-3).
- Schulman, J. H., L. W. Evans, R. J. Ginther, and K. J. Murata, 1947, The sensitized luminescence of manganese-activated calcite: *Journal of Applied Physics*, v. 18, p. 732–739, doi:[10.1063/1.1697831](https://doi.org/10.1063/1.1697831).
- Seal, R. R., 2006, Sulfur Isotope Geochemistry of sulfide minerals: *Reviews in mineralogy and geochemistry*, v. 61, p. 633–677, doi:[10.2138/rmg.2006.61.12](https://doi.org/10.2138/rmg.2006.61.12).
- Secretaría de Energía de la Nación, 2014, Reporte de Producción capítulo IV, accessed July 28, 2014, [www.se.gov.ar/datosupstream/consulta\\_avanzada/listado.php](http://www.se.gov.ar/datosupstream/consulta_avanzada/listado.php).
- Segal, D. B., M. D. Ruth, and I. S. Merin, 1986, Remote detection of anomalous mineralogy associated with hydrocarbon production: Lisbon Valley, Utah. *The Mountain Geology*, v. 23, p. 51–62.
- Shebl, M. A., and R. C. Surdam, 1996, Redox reactions in hydrocarbon clastic reservoirs: Experimental validation of this mechanism for porosity enhancement: *Chemical Geology*, v. 132, p. 103–117, doi:[10.1016/S0009-2541\(96\)00045-9](https://doi.org/10.1016/S0009-2541(96)00045-9).



- Sigismondi, M., and V. Ramos, 2009, El flujo de calor en la cuenca Neuquina: *Petrotecnia*, p. 58–76.
- Silvestro, J., and M. Zubiri, 2008, Convergencia oblicua: Modelo estructural alternativo para la Dorsal neuquina (39°S)-Neuquén: *Revista de la Asociación Geológica Argentina*, v. 63, no. 1, p. 49–64.
- Stipanovic, P. N., F. Rodrigo, O. L. Baulies, and C. G. Martínez, 1968, Las formaciones presenonianas en el denominado Macizo Nordpatagónico y regiones adyacentes: *Revista de la Asociación Geológica Argentina*, v. 23, p. 76–98.
- Surdam, R. C., L. J. Crossey, E. Svenhagen, and H. Heasler, 1989, Organic-inorganic interaction and sandstone diagenesis: *AAPG Bulletin*, v. 73, no. 1, p. 1–23.
- Surdam, R. C., S. J. Zun, and D. B. MacGowan, 1993, Redox reactions involving hydrocarbons and mineral oxidants: A mechanism for significant porosity enhancement in sandstones: *AAPG Bulletin*, v. 77, p. 1509–1518.
- Tucker, M. E., V. P. Wright, and J. A. D. Dickson, 1990, *Carbonate sedimentology*: London, Blackwell, 482 p.
- Tunik, M., A. Folguera, M. Naipauer, M. Pimentel, and V. A. Ramos, 2010, Early uplift and orogenic deformation in the Neuquén basin: Constraints on the Andean uplift from U-Pb and Hf isotopic data of detrital zircons: *Tectonophysics*, v. 489, p. 258–273.
- Uliana, M. A., and K. T. Biddle, 1988, Mesozoic-Cenozoic paleogeographic and geodynamic evolution of southern South America: *Revista Brasileira de Geociências*, v. 18, no. 2, p. 172–190.
- Uliana, M., L. Legarreta, G. Laffite, and H. Villar, 1999, Estratigrafía y geoquímica de las facies generadoras de hidrocarburos en las cuencas petrolíferas de la Argentina: 4° Congreso de exploración y desarrollo de hidrocarburos, Mar del Plata, tomo I, 44 p.
- Van der Kamp, P. C., and B. E. Leake, 1996, Petrology, geochemistry, and Na metasomatism of Triassic–Jurassic non-marine clastic sediments in the Newark, Hartford, and Deerfield rift basins, northeastern USA: *Chemical Geology*, v. 133, p. 89–124, doi:[10.1016/S0009-2541\(96\)00071-X](https://doi.org/10.1016/S0009-2541(96)00071-X).
- Villar, H. J., L. Legarreta, C. Cruz, G. A. Laffiteand, and G. Vergani, 2005, Los cinco sistemas petrolero coexistentes en el sector sudeste de la Cuenca Neuquina: Definición geoquímica y comparación a lo largo de una transecta de 150 km: 6° Congreso de exploración y desarrollo de hidrocarburos, Mar del Plata, 17 p. CD-ROM.
- Walker, T. R., 1976, Red beds in the western interior of the United States: U.S. Geological Survey, Professional Paper 853, p. 49–56.
- Willey, L. M., Y. K. Kharaka, T. S. Presser, J. B. Rapp, and I. Barnes, 1975, Short chain aliphatic acid anions in oil field waters and their contribution to the measured alkalinity: *Geochemical et Cosmochimica Acta*, v. 39, p. 1707–1711, doi:[10.1016/0016-7037\(75\)90092-7](https://doi.org/10.1016/0016-7037(75)90092-7).
- Wood, J. R., and J. R. Boles, 1991, Evidence for episodic cementation and diagenesis recording of seismic pumping events, North Coles Levee, California, U.S.A.: *Applied Geochemistry*, v. 6, p. 509–521, doi:[10.1016/0883-2927\(91\)90050-Y](https://doi.org/10.1016/0883-2927(91)90050-Y).
- Wortmann, U. G., S. M. Böttcher, and S. Bernasconi, 2001, Hypersulfidic deep biosphere indicates extreme sulfur isotope fractionation during single step microbial sulfate reduction: *Geology*, v. 29, p. 647–650, doi:[10.1130/0091-7613\(2001\)029<0647:HDBIES>2.0.CO;2](https://doi.org/10.1130/0091-7613(2001)029<0647:HDBIES>2.0.CO;2).
- Zielinski, R. A., S. Bloch, and T. R. Walker, 1983, The mobility and distribution of heavy metals during the formation of first cycle red beds: *Economic Geology*, v. 78, p. 1574–1589, doi:[10.2113/gsecongeo.78.8.1574](https://doi.org/10.2113/gsecongeo.78.8.1574).